INVESTIGATION OF KINETICS AND EQUILIBRIUM CHARACTERISTICS OF ELECTRICAL DOUBLE LAYER CAPACITORS

by
Yağız Efe Korkmaz
B.S., Physics, Boğaziçi Univeristy, 2021

Submitted to the Institute for Graduate Studies in
Science and Engineering in partial fulfillment of
the requirements for the degree of
Master of Science

Graduate Program in Computational Science and Engineering
Boğaziçi University
2025

ACKNOWLEDGEMENTS

First and foremost, I would like to express my deepest gratitude to my advisor, Assoc. Prof. Betül Uralcan, for her invaluable guidance, unwavering patience, and constant encouragement throughout my master's journey. Her ability to foster an open and supportive environment allowed me to freely express my ideas and develop academically and personally. As a master's student transitioning from a different academic background, her expertise, dedication, and passion for teaching were critical in helping me navigate and grow in this new field.

I am also profoundly thankful to my lab colleagues, Duygu Kaya and Ayşe Saliha Korkut, whose experience and knowledge provided invaluable support during my studies. Their friendship, as well as their professional and emotional support, was essential to my progress. Additionally, I wish to extend my heartfelt thanks to Ayşe Hafsa Doğan, my partner in crime during this incredible journey. From solving complex problems together to sharing countless moments of laughter, she made my master's experience both enriching and enjoyable. I feel fortunate to have had such a wonderful lab partner.

I owe a special debt of gratitude and love to my family, whose unwavering support and trust have been the foundation of my accomplishments. Furthermore, I would like to express my heartfelt thanks to Aleyna Berfin Baykal, my biggest supporter, whose understanding, patience, and encouragement sustained me through the challenges of balancing my academic and personal life.

This work was supported by grants from The Scientific and Technological Research Council of Turkey (TUBITAK) under BIDEB 2232-A International Fellowship for Outstanding Researchers (Project Number T118C220) and Bogazici University Research Fund (Project Number 17841).

ABSTRACT

INVESTIGATION OF KINETICS AND EQUILIBRIUM CHARACTERISTICS OF ELECTRICAL DOUBLE LAYER CAPACITORS

The demand for efficient and scalable energy storage solutions has driven significant advancements in the field of supercapacitors. This study investigates the kinetic and structural equilibrium characteristics of Electrical Double-Layer Capacitors (EDLCs) using molecular dynamics (MD) simulations to explore the effects of pore size, solvent dipole moment, and applied voltage on their performance. Twenty systems were designed, combining two pore sizes (7.78 Å and 14.75 Å), five solvent dipole moments (0.91 D to 6.18 D), and two applied voltages (1 V and 2 V). The study aims to elucidate the interplay of these parameters in optimizing the energy and power densities of EDLCs. The results reveal that pore sizes and electrode voltages has a complex and sensitive relation with the capacitance. For systems with a 14.75 Å pore size, a positive correlation between dipole moment and capacitance was observed across all dipole moments. However, for narrower pores (7.78 Å), this correlation reversed beyond a dipole moment of 2.88 D, highlighting the complex dependence of capacitance on solvent polarity. Additionally, the behavior of the electrolyte within the pores showed distinct spatial distributions, with narrower pores exhibiting denser ion layering and wider pores facilitating more uniform ion dispersal. This research contributes to a deeper understanding of EDLC dynamics, offering actionable insights for the design of next-generation supercapacitors.

ÖZET

ELEKTRİK ÇİFT TABAKA KAPASİTÖRLERİNİN KİNETİK VE DENGE ÖZELLİKLERİNİN İNCELENMESİ

Günümüzde enerji depolama sistemlerine olan ihtiyaç, enerji verimliliğini ve ölçeklenebilirliği artırmayı hedefleyen önemli gelişmelere öncülük etmiştir. Bu bağlamda, süperkapasitörler ve özellikle Elektrik Çift Tabaka Kapasitörleri (EDLC'ler), hem teorik hem de pratik anlamda büyük bir araştırma ve geliştirme potansiyeli sunmaktadır. Bu çalışmada, EDLC'lerin kinetik ve yapısal denge özellikleri, Moleküler Dinamik (MD) simülasyonları kullanılarak detaylı bir şekilde incelenmiştir. Çalışmada, gözenek boyutu (7.78 Å ve 14.75 Å), çözücü dipol momenti (0.91 D ile 6.18 D arasında) ve uygulanan voltaj (1 V ve 2 V) gibi parametrelerin performans üzerindeki etkileri değerlendirilmiştir. Toplamda yirmi farklı sistem simüle edilmiş ve bu parametrelerin EDLC'nin enerji ve güç yoğunluklarını nasıl etkilediği analiz edilmiştir. Sonuçlar, gözenek boyutu ve elektrot voltajının kapasitans ile karmaşık ve hassas bir ilişki içinde olduğunu göstermektedir. 14.75 Å gözenek boyutuna sahip sistemlerde, çözücü dipol momenti ile kapasitans arasında tutarlı bir pozitif ilişki gözlemlenmiştir. Ancak, dar gözenek boyutuna sahip sistemlerde (7.78 Å), bu ilişki 2.88 D'den yüksek dipol momentlerinde tersine dönmüş ve kapasitansın çözücü polaritesi ile karmaşık bir ilişkiye sahip olduğu ortaya konmuştur. Buna ek olarak, gözenek içindeki elektrolit davranışları, iyonların dağılımlarında önemli farklılıklar sergilemiştir. Dar gözenekler yoğun iyon tabakalaşması gösterirken, geniş gözenekler daha homojen bir iyon dağılımını desteklemiştir. Bu bulgular, EDLC'lerin performansını artırmak için gözenek boyutu, çözücü polaritesi ve uygulanan voltaj gibi yapısal ve elektrokimyasal parametrelerin dikkatli bir şekilde optimize edilmesi gerektiğini göstermektedir.

TABLE OF CONTENTS

LIST OF FIGURES

LIST OF TABLES

LIST OF SYMBOLS

A	Area
C	Capacitance
D	Diffusion coefficient
E_T	Total potential energy
F_i	Force acting on a particle
k	Wave number
k_b	Bond force constant *or* Boltzmann constant
m	Mass
M	Dipole moment
p_{a-c}	Ion polarization
q_i	Charge of a particle
Q	Total charge
r	Current bond length
r_0	Reference bond length
r_i	Position vector
t	Time
$U(r_i)$	Potential Energy Function
V_0	Constant applied voltage
ΔF	Free Energy
Δz	Thickness
ϵ_0	Medium permittivity
ϵ_{eff}	Effective dielectric constant
γ	Phase angle
l	Charge density correlation length
ϕ	Dihedral angle
Φ	Electrical Potential
Π	Rectangular function

ρ_n	Number Density
ρ_q	Charge Density
σ	Collision diameter
τ	Characteristic time
θ	Current bond angle
θ_0	Reference bond angle
ξ	Effective charge separation

LIST OF ACRONYMS/ABBREVIATIONS

AC	Active Carbon
ACN	Acetonitrile
CNT	Carbon Nanotube
ECS	Effective Charge Separation
EDC	Effective Dielectric Constant
EDLC	Electrical Double Layer Capacitor
WiSE	Water-in-Salt Electrolytes
MD	Molecular Dynamics
MSD	Mean Squared Displacement
PPPM	Particle Particle Particle Mesh
RTIL	Room Temperature Ionic Liquid
SSA	Specific Surface Area

1. INTRODUCTION

In recent decades, the demand for efficient, sustainable, and scalable energy storage technologies has emerged as one of the most critical challenges in scientific and engineering research [1]. This growing necessity is driven by global trends such as the increased adoption of renewable energy sources, the electrification of transportation systems, and the continuous evolution of smart grids. To support these advancements, energy storage systems must satisfy stringent requirements for efficiency, scalability, and adaptability across diverse applications.

Traditional energy storage solutions, including batteries [2] and conventional capacitors, have historically underpinned various technologies. In a battery, energy storage is achieved through electrochemical reactions occurring between two electrodes typically referred to as the anode and cathode—immersed in an electrolyte. When a voltage is applied, oxidation and reduction reactions take place at the respective electrodes, leading to the movement of electrons through an external circuit and ions through the electrolyte. This process enables the storage of chemical energy, which can later be converted into electrical energy when the battery is discharged. Once the circuit is completed, the stored energy is released as electrons flow from the anode to the cathode, driving the connected load. In a traditional capacitor, energy storage is achieved through two conducting plates (electrodes) separated by a dielectric material (insulator). When voltage is applied, an electric field forms across the dielectric, leading to the accumulation of negative charges (electrons) on one plate and positive charges (holes) on the other. The resulting charge separation facilitates energy storage. Once charged, the capacitor retains its stored energy until it is discharged through a connected circuit [3]. The electrodes are typically composed of materials like thin metal films, disks, or aluminum foil, with the shape and size of the plates varying depending on the application. For example, cylindrical plates are often preferred in devices that require compact, high-capacitance components, such as electric motors and industrial machinery.

However, these systems face inherent limitations, such as the relatively slow charge-discharge cycles of batteries and the low energy density of capacitors [4]. These shortcomings have catalyzed a shift toward novel electrochemical energy storage devices that address these challenges. Among these innovations, electric double-layer capacitors (EDLCs), commonly referred to as supercapacitors, have emerged as a promising alternative, effectively bridging the performance gap between batteries and capacitors. A comparison figure due to their energy and power density representation of energy storage technologies is given below for capacitors, supercapacitors, batteries, fuel cells and a combustible engines.

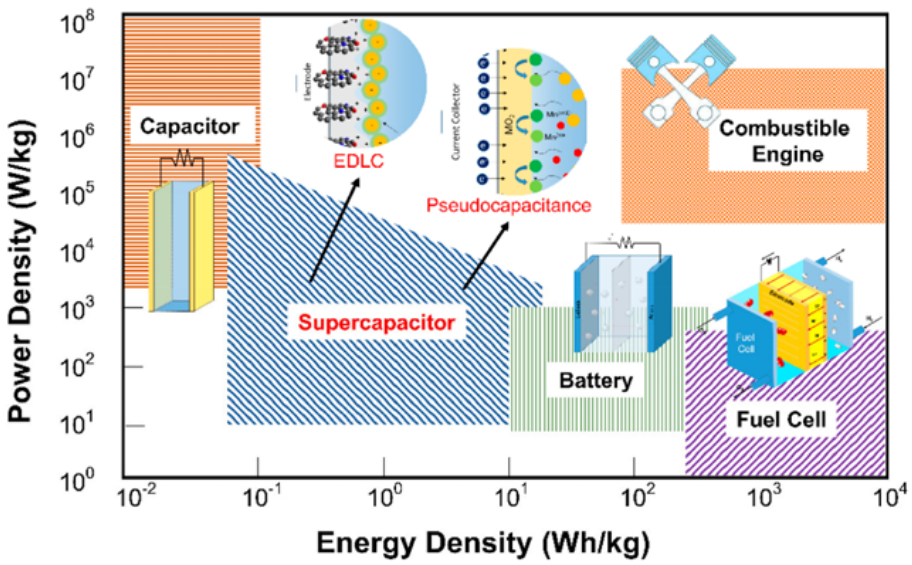

Figure 1.1. Comparison between energy storage technologies due to their average Energy and Power Density. The figure is taken from [5].

Supercapacitors stand out due to their ability to rapidly store and release energy, exceptional cycle life, and robust operational safety under a broad range of conditions [6]. These features have made them indispensable for high-power applications, including regenerative braking systems in electric and hybrid vehicles, pitch control systems in wind turbines, and uninterruptible power supplies in critical infrastructure [7]. Given these advantages, supercapacitors are poised to play a significant role in the future of energy storage and utilization. Their potential to seamlessly integrate into

everyday life suggests a growing presence in both industrial and consumer applications in the years to come.

Supercapacitors are categorized into three distinct types based on their charge storage mechanisms: (1) non-Faradaic, utilized in EDLCs where energy is stored through electrostatic interactions, (2) Faradaic, characteristic of pseudocapacitors that rely on redox reactions, and (3) hybrid supercapacitors, which combine both non-Faradaic and Faradaic processes [8–10]. A critical factor in determining the charge storage mechanism of a supercapacitor is the selection of electrode materials. For instance, carbon-based materials such as activated carbon (AC), graphene, and carbon nanotubes (CNTs) are predominantly employed for non-Faradaic processes due to their high surface area and excellent conductivity. In contrast, materials like metal oxides, conducting polymers, and certain non-metal oxides are typically associated with Faradaic charge storage mechanisms.

1.1. Fundamental Features of EDLCs

Structurally, EDLCs resemble conventional batteries as they consist of two electrodes immersed in an electrolyte. These electrodes are separated by ion-conductive porous structures or ion-conductive membranes, which prevent electrical short circuits within the device. When an external voltage is applied, charges accumulate on the surfaces of the electrodes. This accumulation is counterbalanced by the adsorption of oppositely charged ions from the electrolyte. The resulting charge separation at the electrode/electrolyte interface generates capacitance (C). A schematic illustration of the EDLC charging process is presented below.

To form the electric double layer illustrated in Figure 1.2, a variety of carbon-based materials with high porosity have been utilized, including activated carbon (AC) [11,12], carbon nanotubes (CNTs) [13], graphene [14], carbon aerogels [15], carbon foam [16], and carbide-derived carbon [17, 18]. The application of these carbon-based materials in electric double-layer capacitors (EDLCs) provides remarkable charge-discharge

stability, with a lifespan of approximately 28,000 cycles [19], and outstanding capacity retention exceeding %90 after thousands of cycles [13, 20].

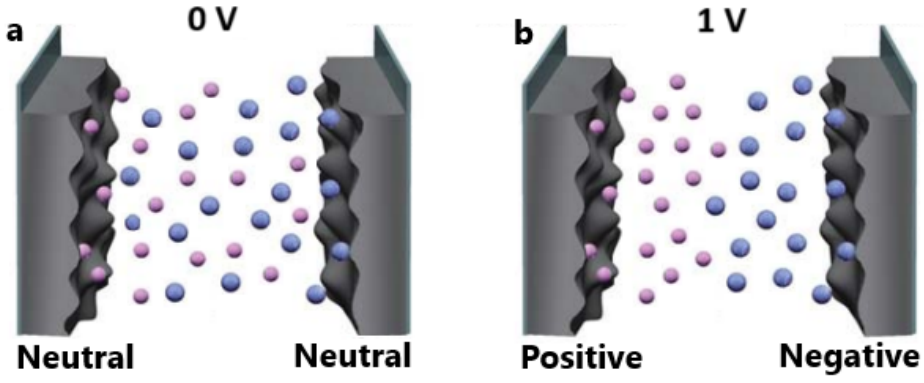

Figure 1.2. Schematic representation of the charging mechanism of an EDLC electrode. (Pink particles represent anions and blue particles represent cations) (a) Before the applied voltage (b) After the applied voltage.

Among the various electrode materials available for use in EDLC systems, graphene sheets have been selected as the electrode layers in this study. Graphene, a two-dimensional material consisting of a single atomic layer of carbon atoms, as depicted in Figure 1.3, has gained significant attention as a promising candidate for EDLC applications due to its exceptional properties, including high electrical conductivity, chemical stability, and a large surface area [12, 21, 22].

Unlike other carbon-based materials such as carbon nanotubes, activated carbon, and carbide-derived carbon, the performance of graphene as an EDLC electrode material is not constrained by the distribution of pores within its solid structure [23]. Furthermore, graphene exhibits a significantly higher specific surface area (SSA) of approximately 2630 m^2/g [24]. When fully utilized, this SSA enables graphene to achieve a theoretical capacitance of up to 550 F^2/g [21]. Additionally, graphene's structure allows both major surfaces to be exposed and readily accessible to the electrolyte, further enhancing its efficiency as an electrode material.

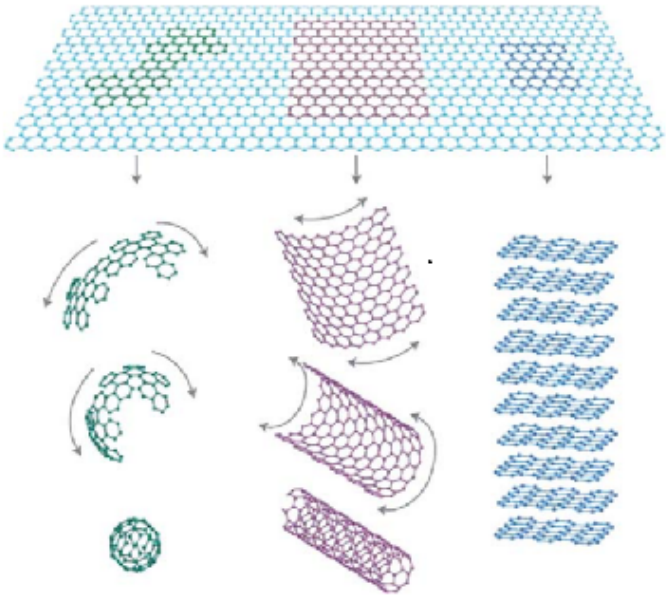

Figure 1.3. Representation of a graphene sheet that can be form in different shapes to use as an electrode in different types of EDLCs. The figure is taken from [25].

1.2. Understanding EDLC Dynamics and Enhancing EDLC Performance

Ultimately, irrespective of their type, the primary objective of all energy storage devices is to store energy and release it when required. To evaluate and understand the performance of an EDLC, two critical performance metrics are commonly used: (a) energy density and (b) power density. Energy density (E) represents the amount of energy an EDLC can store per unit volume or mass, as defined in below. Power density (P), on the other hand, quantifies the rate at which an EDLC can deliver its stored energy, also expressed per unit volume or mass and they are expressed as

$$E = \frac{1}{2}CV^2 \tag{1.1}$$

$$P = \frac{V^2}{Rm} \tag{1.2}$$

where V denotes the applied voltage across the electrodes, C represents the capacitance of the EDLC, R is the resistance, and m is the active mass of the electrode. Although Equations 1.1 and 1.2 indicate that the energy and power densities of an EDLC are

directly proportional, a trade-off often exists between these two metrics. This trade-off arises due to the inherent limitations of electrode material properties and ion transport dynamics [26].

As evident from Equation 1.1, the energy stored in an EDLC is directly and positively correlated with its capacitance. Consequently, C is a critical parameter for an Electrical Double Layer Capacitor (EDLC), as it directly determines the device's energy storage capability. The capacitance is expressed as

$$C = \frac{A\epsilon_0\epsilon_r}{d} \tag{1.3}$$

where A represents the surface area of the electrode accessible to the electrolyte, ϵ_0 is the vacuum permittivity (8.85×10^{-12} F/m), ϵ_r is the dielectric constant of the electrolyte (relative to ϵ_0), and d denotes the average distance between the ions and the electrode surface.

Although EDLCs demonstrate remarkable specific capacitance and power density compared to conventional capacitors, their widespread adoption has been hindered by their relatively low energy density. This limitation arises from their charge storage mechanism, which relies on non-faradaic reactions, especially when compared to conventional electrochemical energy storage devices such as batteries [27]. Among the three primary types of supercapacitors, pseudocapacitors, and hybrid supercapacitors, EDLCs exhibit the lowest energy density. Overcoming this limitation and optimizing energy storage performance require the identification, design, and development of supercapacitors that facilitate rapid charge transport and enhanced capacitance [28–30].

In the pursuit of enhancing the energy density of supercapacitors, considerable attention has been directed toward the intrinsic properties of electrode shape and materials, as well as electrolytes, which govern supercapacitor performance. Concerning electrode shape and materials, the incorporation of nanoporous carbon-based materials as novel electrodes, characterized by increased specific surface areas, [22, 31, 32] presents a promising avenue to overcome the moderate energy density associated with supercapacitors. The interplay between pore size and surface properties of these ma-

terials plays a pivotal role in determining their effectiveness in boosting energy density [33–40]. Regarding the concept, McDaniel et al. [41] researched five distinct carbon nanotube/graphene composite electrodes, investigating the effects on capacitance under varying voltage conditions. Their findings reveal that at lower voltages, the differential capacitance values of various electrode structures exhibit minor variations. However, beyond an applied voltage of 1 V, the electrode with the highest surface area surpasses other structures in terms of capacitance by approximately 40%.

In addition to the electrode characteristics discussed above, the electrolyte selection and the interplay between electrolyte properties and pore size are critical in determining the overall capacitance of EDLCs. Broadly, four classes of electrolytes are commonly utilized in supercapacitors: aqueous, organic solvent–based, water-in-salt, and room-temperature ionic liquid (RTIL)–based electrolytes. Each of these electrolyte types offers a distinctive balance of advantages and drawbacks:

(i) Aqueous Electrolytes: Aqueous solutions (often acidic or alkaline) typically provide high ionic conductivity, which can translate to low internal resistance and good power performance. However, their narrow electrochemical stability window (usually below 1.2 V) restricts the operating voltage and thus limits energy density. Additionally, corrosion and side reactions may occur at higher voltages, curtailing the long-term stability of such systems.

(ii) Organic Solvent–Based Electrolytes: Organic solvents (e.g., acetonitrile or propylene carbonate) exhibit a wider voltage window (up to 2.7–3.0 V) compared to aqueous counterparts. This wider electrochemical stability range can significantly enhance energy density. Nonetheless, organic solvents can be flammable, more expensive, and sometimes more toxic than water-based systems. Additionally, certain organic electrolytes have higher viscosities or lower conductivities, influencing ion mobility and hence the capacitor's charging–discharging rate.

(iii) Water-in-Salt Electrolytes: A more recent development involves highly concentrated aqueous electrolytes, often termed "water-in-salt" solutions [42]. By substantially increasing the salt concentration, the effective electrochemical stability

window of water can be extended beyond the conventional 1.2 V limit. This approach can provide improved energy density and retain the high ionic conductivity characteristic of aqueous systems. However, the large salt content may raise costs and introduce complexities related to salt solubility and viscosity at high concentrations.

(iv) Room-Temperature Ionic Liquid (RTIL)–Based Electrolytes: RTILs, formed by bulky organic cations coupled with various anions, feature excellent electrochemical stability, negligible vapor pressure, and non-flammability [43, 44]. These attributes allow for broader operating voltage ranges and improved safety. However, as highlighted earlier, pure RTILs often suffer from higher viscosity and reduced ionic conductivity, especially under lower temperatures [45]. Consequently, charging–discharging kinetics may slow down in nanoporous electrodes.

To investigate the impact of an ionic liquid (IL) on capacitance, Tu et al. [44] worked on EDLCs and performed molecular dynamic simulations for three distinct ionic liquid compositions involving 1-butyl-3-methylimidazolium ($BMIM^+$) cations paired with bistriflimide ($TFSI^-$), triflate (OTF^-), or tetrafluoroborate (BF_4^-) anions. Their results indicate that all three ionic liquid compositions exhibit distinct behaviors as the voltage increases. Notably, [$BMIM^+$][$TFSI^-$] demonstrates a significant 2–3 times enhancement in capacitance, whereas the other two ILs show a much smaller increase in capacitance.

Despite these positive attributes of RTILs, challenges arise when using pure RTILs as electrolytes for EDLCs, such as high viscosity affecting charging and discharging rates, [45] resulting in decreased conductivity. To address these issues and enhance electrolyte transportation performance, the organic solvent is added to the ionic liquid, as the presence of organic solvent negatively impacts anion-cation interactions, leading to lower viscosity and higher ionic conductivity [36, 46–53]. This improvement is not a binary effect solely attributable to the presence of organic solvent; rather, it varies with solvent type [46, 54], concentration [55–57] and dipole moment [58–63].

The study conducted by Smith et al. [64] holds significance in comprehending electric fields and surface forces in concentrated electrolytes. Their research highlights a positive correlation between the electrostatic screening length and ion concentration beyond the dilute regime. Furthermore, they concluded that scaling the screening lengths by the dielectric constants results in a collapse of their curves into one. Lee et al. [65] elucidate this nonmonotonic behavior by proposing a simple scaling theory. Coles et al. [66] complement recent experimental findings through all-atom explicit-solvent MD simulations, establishing a universal scaling law that the screening length adheres to in concentrated regimes. However, it is noteworthy that their scaling exponent is significantly lower than the one observed in experimental studies.

In this study, a deeper investigation is conducted into the impact of pore size in the porous carbon electrode, solvent polarity, and applied voltage on EDLC performance. Recently, several studies have been conducted concerning these parameters. Regarding the pore size, Uralcan et al. [57] indicate that larger pore sizes lead to a reduction in charging time, yet capacitance exhibits nonmonotonic behavior with varying pore size. Kondrat et al. [37] also propose that the energy density is a non-monotonic function of pore size, and its maximum depends on the applied voltage. Furthermore, Lin et al. [46] observe that, in the course of partial dissolvation during the charging process, distinct solvent molecules exhibiting specific polarities may demonstrate more efficient responses to varying pore sizes in relation to capacitance.

In terms of the effect from solvent polarity to capacitance, Osti et al. [60] experimentally studies the effects of different solvent dipole moments on anion-cation interactions and kinetic properties. For different pore sizes, Decaux et al. [59] investigate the performance of two different cation-solvent pairs (Li^+ and TEA^+ as cations, alkyl carbonates and ACN as solvents) with different polarities and concludes that the pair with a higher polarity keeps its solvation shell and therefore needs a wider pore.

These studies suggest that the combined effects of electrode pore size, solvent polarity, and applied voltage play a significant role in EDLC performance. To in-

vestigate these parameters comprehensively, molecular dynamics (MD) simulations of EDLC systems are conducted using varied combinations of pore size, dipole moments of organic solvents, and applied electrode voltages. These simulations aim to analyze the kinetic and structural properties of EDLCs under different conditions.

1.3. Molecular Dynamics Simulations of EDLCs

In the quest to enhance the performance of Electrical Double Layer Capacitors (EDLCs), understanding the interactions between electrode materials and electrolytes at the molecular level is of utmost importance. Classical molecular dynamics (MD) simulations provide a powerful tool to investigate how pore (or pore-size) effects and different electrolyte types (aqueous, organic solvent-based, water-in-salt, and room-temperature ionic liquid, RTIL) influence capacitance. Below, we outline key MD-based studies on these four electrolyte categories and then focus on RTIL/organic solvent mixtures in particular.

The choice of electrolyte significantly affects the formation and behavior of the electric double layer (EDL) at the electrode interface. Computational studies have extensively explored four main classes of electrolytes: aqueous solutions, organic solvent-based electrolytes, water-in-salt electrolytes (WiSEs), and room-temperature ionic liquid (RTIL)-based systems.

(i) Aqueous Electrolytes: MD simulations have revealed that aqueous electrolytes exhibit high ionic conductivity and relatively low viscosity, leading to fast ion transport [67,68]. However, the primary drawback is their limited electrochemical stability window (typically 1.23 V), which restricts the achievable energy density. [48]

(ii) Organic Solvent-Based Electrolytes: These electrolytes, such as acetonitrile, offer a wider electrochemical window (2.5–3 V) compared to aqueous solutions. However, computational studies indicate that their higher viscosity can impede ion mobility, leading to slower EDL formation [37, 43].

(iii) Water-in-Salt Electrolytes (WiSEs): WiSEs have emerged as a promising class due to their expanded electrochemical window (3 V) while maintaining a water-based system. MD simulations suggest that the structuring of these highly concentrated solutions leads to unique solvation environments that impact ion dynamics and EDL formation [69, 70].

(iv) Room-Temperature Ionic Liquids (RTILs): RTILs are extensively studied due to their intrinsic wide electrochemical window, non-volatility, and high thermal stability. MD simulations have revealed that RTILs exhibit strong ion-pairing and layered structuring near the electrode, which can both enhance and limit capacitance depending on pore size and ion desolvation effects [67].

Within the realm of RTIL-based electrolytes, the specific choice of ionic liquid can significantly impact charge storage behavior. Computational studies have investigated the interplay between cation-anion pairing, ion size, and transport dynamics:

RTIL Structure and Ion Dynamics: MD simulations have shown that RTILs with asymmetric cations or weaker ion-ion interactions facilitate better ion transport and improved EDL formation, while highly structured RTILs may suffer from sluggish dynamics [71].

Pore Size-RTIL Type Interactions: Studies indicate that RTILs with smaller, less bulky ions exhibit better penetration into nanoporous electrodes, whereas larger RTIL ions require optimized pore sizes to achieve maximum capacitance [72].

One of the most extensively investigated topics in computational electrochemistry is the effect of organic solvent addition to RTIL-based electrolytes. MD simulations have provided valuable insights into the molecular-scale interactions that govern these mixed systems:

Solvent-Induced Changes in RTIL Structuring: The structuring of room-temperature ionic liquids (RTILs) in the presence of organic solvents plays a crucial role in deter-

mining their electrochemical behavior in supercapacitors. Molecular dynamics (MD) simulations have provided valuable insights into how solvents influence ion distribution, conductivity, and capacitance. Recent studies have investigated these effects in various RTIL-solvent systems and different electrode configurations.

Pivnic et al. explored the structural forces in RTIL-organic solvent mixtures, highlighting how solvent-induced screening effects alter ion correlations and impact electrochemical stability [47]. Similarly, Shim et al. conducted MD simulations on graphene-based supercapacitors, demonstrating that RTIL structuring at the electrode interface significantly influences charge storage efficiency [73]. In another study, Chaban et al. examined the role of acetonitrile as a co-solvent, finding that it enhances ionic mobility and boosts overall conductivity in imidazolium-based RTILs, thereby improving supercapacitor performance [51]. Shim et al. compared the behavior of ionic liquids and organic electrolytes in a parallel-plate graphene-based supercapacitor configuration, showing that solvent selection directly impacts ion layering, charge dynamics, and energy storage efficiency [52]. In another study, Li et al. investigated the impact of adding organic solvents, such as acetonitrile (ACN) and ethylene carbonate (EC), to tricationic ionic liquids [74]. Their findings revealed that solvent addition significantly reduces ion interactions, thereby enhancing ion diffusion and conductivity. Notably, the differential capacitance-voltage profile maintained its asymmetric camel shape, indicating that solvent incorporation improves power density without compromising energy storage capabilities. The addition of organic solvents like acetonitrile has also been found to reduce viscosity and disrupt strong ion-ion interactions, leading to enhanced ion mobility and more efficient charge storage [75].

These studies collectively demonstrate that solvent-induced modifications in RTIL structuring significantly influence ion transport, capacitance, and energy storage properties. Understanding these interactions at the molecular level is essential for optimizing RTIL-based electrolytes for next-generation supercapacitors.

Optimizing Solvent Ratios: The performance of supercapacitors is highly dependent on the electrolyte composition, particularly the ratio of solvents in ionic-liquid-based electrolytes. Molecular dynamics (MD) simulations have been instrumental in understanding how solvent concentration influences ion distribution, charge storage, and overall capacitive behavior.

Zhang et al. [55] investigated the effects of solvent concentration on the performance of ionic-liquid/carbon supercapacitors, demonstrating that an optimal solvent ratio can enhance ion mobility and improve capacitance by reducing ion aggregation. Their study highlighted the delicate balance between solvent-mediated screening effects and ion-pore interactions that govern charge storage efficiency. Similarly, Uralcan et al. explored concentration fluctuations in dense ionic solutions and their impact on capacitive response, showing that solvent-induced variations in ion structuring play a critical role in determining energy and power density [56]. Their findings suggest that fine-tuning solvent concentrations can lead to significant improvements in electrochemical performance.

Pore Size Dependence in Mixed Systems: The pore size of electrode materials plays a crucial role in determining the electrochemical performance of supercapacitors. In mixed solvent and ionic liquid systems, the interaction between pore size and electrolyte structuring can lead to non-trivial effects on capacitance, charge distribution, and energy storage efficiency.

Péan et al. explored the dynamics of charging in nanoporous carbon-based supercapacitors, revealing that charge storage mechanisms are highly dependent on pore size and ion confinement [38]. Their study showed that while small pores enhance ion packing, they also introduce longer charging times due to steric hindrance. Similarly, Jiang et al. investigated the solvent effect on pore-size dependence in organic electrolyte supercapacitors, demonstrating that solvent molecules mediate ion accessibility to pores, leading to tunable capacitance trends [35]. Their findings suggest that optimal solvent selection can mitigate size-exclusion effects and enhance charge efficiency.

Lastly, Feng et al. showed that supercapacitor capacitance exhibits an oscillatory behavior as a function of nanopore size, highlighting the complex interplay between ion layering, electrode curvature, and electrolyte structuring [36]. This oscillatory trend indicates the presence of critical pore sizes that maximize charge storage efficiency.

These studies collectively emphasize the intricate relationship between pore size and electrolyte behavior in mixed systems, providing crucial insights for designing high-performance supercapacitors. Optimizing pore-electrolyte interactions through tailored nanostructuring and solvent selection is essential for advancing energy storage technologies.

These computational findings, categorized as above, collectively highlight the intricate interplay between electrolyte composition, pore size, and ion dynamics, reinforcing the importance of molecular-scale studies in optimizing EDLC performance.

2. COMPUTATIONAL METHODS

In this section, the materials and methods employed to construct, execute, and analyze an EDLC molecular dynamics simulation system are presented. This includes a detailed description of the simulation setup, the parameters utilized, the computational techniques applied, as well as the mathematical and statistical methods used to analyze the system's kinetic and structural properties.

2.1. Mathematical Insights on Molecular Dynamic Simulations

As described in Section 1.3, molecular dynamics (MD) simulations are powerful and versatile tools for studying the physical movements of atoms and molecules. Various types of MD simulations can be employed depending on the research objectives, including classical MD, ab initio MD, coarse-grained MD, and reactive MD. Each type is characterized by its level of detail and the mathematical principles governing the interactions within the system.

In classical MD simulations, the prediction of the next simulation step is based on the parameters of the current step, as governed by Newton's equations of motion. The interactions between particles within the system are calculated using empirical force fields, such as Coulombic interactions or Lennard-Jones potentials, which approximate the forces acting on the particles.

In this study, classical MD methods and Lennard-Jones potentials were utilized to simulate various EDLC systems. A brief overview of the mathematical framework underlying classical MD is provided below.

Classical molecular dynamics (MD) is founded on Newton's Second Law, which describes the relationship between the force applied to an object and the resultant acceleration. The law is expressed as:

$$m_i \frac{d^2 r_i}{dt^2} = F_i \tag{2.1}$$

where m_i is the mass, r_i is the position vector and F_i is the force acting on the i-th particle. In the context of MD simulations, the force acting on each particle is derived from the gradient of the potential energy function U(r), such that:

$$F_i = -\nabla U(r_i) \tag{2.2}$$

where $U(r_i)$ is the potential energy function. By integrating this equation of motion over time, the trajectory of each particle in the system can be determined. The output of the n-th trajectory serves as the input for the $n+1$-th trajectory, allowing the simulation to progress iteratively over a specified period of time.

As shown in Equation 2.1 and Equation 2.2, the potential energy function, $U(r_i)$, is fundamental in modeling the interactions among particles, such as ions, solvent molecules, and electrode surfaces. This function is typically expressed as a sum of multiple terms, each representing a specific type of interaction within the system:

$$U(r) = U_{LJ} + U_{bonded} + U_{Coulomb} + U_{external} \tag{2.3}$$

Here, U_{LJ} denotes the non-bonded Van der Waals interactions, which account for short-range repulsion and long-range attraction between particles. These interactions are modeled using the Lennard-Jones potential:

$$U_{LJ}(r) = 4\epsilon \left[\left(\frac{\sigma}{r}\right)^{12} - \left(\frac{\sigma}{r}\right)^{6} \right], \quad r < r_c \tag{2.4}$$

For particle separations exceeding r_c, the Lennard-Jones potential is neglected due to its diminished magnitude and the associated computational costs. Consequently, r_c serves as the cut-off distance for $U_{LJ}(r)$. The parameter ϵ determines the strength of the interaction between two particles, while σ represents the collision diameter, indicating the distance at which the interparticle potential is zero. Essentially, σ defines the effective size of the particles. For interactions between different types of particles, ϵ

and σ are calculated as:

$$\epsilon_{ij} = \sqrt{\epsilon_i \epsilon_j}, \quad \sigma_{ij} = \sqrt{\sigma_i \sigma_j} \tag{2.5}$$

The second term in Equation 2.3 (U_{bonded}) describes the total potential energy arising from bonded interactions between particles: bond stretching, bond bending, and bond torsion. Therefore:

$$U_{\text{bonded}} = \sum U_{\text{bond}}(r) + \sum U_{\text{angle}}(\theta) + \sum U_{\text{torsion}}(\phi) \tag{2.6}$$

The three components that sum up to U_{bonded} are given as follows:

$$U_{\text{bond}}(r) = \frac{k_b}{2}(r - r_0)^2 \tag{2.7}$$

$$U_{\text{angle}}(\theta) = \frac{k_\theta}{2}(\theta - \theta_0)^2 \tag{2.8}$$

$$U_{\text{torsion}}(\phi) = \frac{V_n}{2}\left[1 + \cos(n\phi - \gamma)\right] \tag{2.9}$$

For $U_{\text{bond}}(r)$, r represents the instantaneous bond length, r_0 is the equilibrium bond length, and k_b is the bond force constant or bond stiffness. For $U_{\text{angle}}(\theta)$, θ denotes the instantaneous bond angle, θ_0 is the equilibrium bond angle, and k_θ is the angle force constant. For $U_{\text{torsion}}(\phi)$, ϕ represents the dihedral angle, V_n is the torsional barrier height, n is the periodicity of the torsion, and γ is the phase angle, which determines the potential offset.

Considering the third term in Equation 2.3 (U_{Coulomb}), it represents the Coulomb potential, which models the electrostatic interactions between charged particles in the simulation system. Its formula is given by:

$$U_{\text{Coulomb}}(r) = \frac{1}{4\pi\epsilon_0}\frac{q_1 q_2}{r} \tag{2.10}$$

Here, $\frac{1}{4\pi\epsilon_0}$ is Coulomb's constant, expressed in terms of the permittivity of free space ϵ_0, q_1 and q_2 are the charges of the interacting particles, and r is the distance between these charged particles.

The last term in Equation 2.3 is external potentials (U_{external}). In an EDLC, $U_{external}$ source from the applied voltage to electrodes and can be shown as:

$$U_{\text{external},i} = q_i \Phi_i \tag{2.11}$$

where q_i is the charge of a i-th particle and Φ_i is the electric potential at the position of i-th particle. For an EDLC system, the electric potential Φ_i can be calculated by solving the Poisson's equation below:

$$\nabla^2 \Phi = -\frac{\rho}{\epsilon} \tag{2.12}$$

where $\nabla^2 \Phi$ is the Laplacian of the potential Φ, ρ is the charge density and ϵ is the medium permittivity. For the constant potential simulations, such as in this study, Equation 2.11 becomes much more simple and can be shown as

$$U_{\text{external},i} = q_i V_0, \quad \text{since} \quad \Phi_i = V_0 \tag{2.13}$$

To maintain a constant applied voltage on the electrodes and execute a constant potential molecular dynamics (MD) simulation for an EDLC system, the primary objective is to calculate the charge of all electrode particles accordingly. The individual charges of the electrode particles are adjusted such that they minimize the total potential energy (E_T) of the system which can be expressed as

$$E_T = E_{\text{Coulomb}} - V_0 \sum q_i \tag{2.14}$$

To calculate the charges (q_i) of the electrode particles individually, ensuring that the total potential energy (E_T) of the system is minimized, the matrix inversion method is used in this study [76].

2.2. Simulation System Properties

In this study, the combined effects of electrode pore size, solvent polarity, and the constant voltage applied to the electrode are investigated in an EDLC system. To create the systems, the ionic liquid 1-butyl-3-methylimidazolium hexafluorophosphate $[BMIM^+][PF_6^-]$ and the organic solvent acetonitrile (ACN) are used. The ionic liquid, dissolved in the solvent at a concentration of 3.5 M, serves as the electrolyte. All species are represented using coarse-grained models, with the cations and solvent molecules

maintained in a rigid state.

The dipole moment of the solvent in the respective systems is varied to scrutinize the impact of solvent polarity. This adjustment involves proportionally modifying the charges associated with the ACN solvent model particles to achieve specific dipole moments ranging from 0.91 D to 6.18 D. The cutoff distance for Lennard-Jones interactions is set to 12 Å. The particle-particle particle-mesh (PPPM) solver is employed for Coulombic interactions, and the Lorentz-Berthelot mixing rules are applied to compute cross-parameters. Additional force field parameters used in the simulations are provided in Table 2.1.

Table 2.1. Force field parameters for $[PF_6^-]$ (A), $[BMIM^+]$ (C1, C2, C3) [77], ACN (ME, CA, N) [78] and electrode carbon (C) . There are five different charge combinations for the solvent since different dipole moments are used in different simulation setups.

	A	**C1**	**C2**	**C3**
m (g/mol)	144.96	67.07	15.04	57.12
q (e)	-0.7800	0.4374	0.1578	0.1848
$\boldsymbol{\sigma}$ **(Å)**	5.06	4.38	3.41	5.04
$\boldsymbol{\epsilon}$ **(kcal/mol)**	1.126	0.612	0.086	0.437
	ME	**CA**	**N**	**C**
m (g/mol)	15.04	12.01	14.01	12.01
$\boldsymbol{q_{0.91}}$ **(e)**	0.0594	0.0285	-0.0879	-
$\boldsymbol{q_{2.07}}$ **(e)**	0.1345	0.0645	-0.1990	-
$\boldsymbol{q_{2.88}}$ **(e)**	0.1880	0.0902	-0.2782	-
$\boldsymbol{q_{4.12}}$ **(e)**	0.2690	0.1290	-0.3980	-
$\boldsymbol{q_{6.18}}$ **(e)**	0.4035	0.1935	-0.5970	-
$\boldsymbol{\sigma}$ **(Å)**	3.60	3.40	3.30	3.37
$\boldsymbol{\epsilon}$ **(kcal/mol)**	0.380	0.100	0.100	0.055

The other main component of the simulation setup is the electrodes. There are numerous choices for electrodes in an EDLC system. In this study, slit-pore carbon electrodes are used, consisting of three layers of carbon atoms arranged in a honeycomb lattice to model graphene sheets. The electrode structure used in the simulations is shown in Figure 2.1.

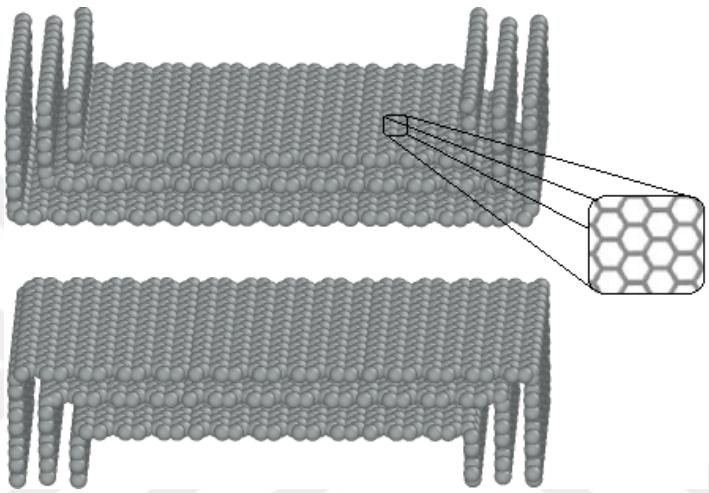

Figure 2.1. Simulation structure of the electrode; Three layered carbon sheets arranged as honeycomb lattice.

The distance between the layers of graphene sheets that form the electrode is 3.38 Å, and the carbon atoms within the graphene sheets are placed at a distance of 1.43 Å from each other. The dimensions of the electrode are 32 Å, 44 Å, and 60 Å in the x, y, and $z$directions, respectively. The electrode pore widths are 7.78 Å and 14.75 Å for different setups.

After the creation of simulation components (electrolytes, solvents and electrodes), the simulation system is created via PACKMOL [79] by determining its dimensions as 32 Å, 44 Å, and 325 Å in the x, y, and z directions, respectively. Then electrodes are placed in fixed positions and electrolytes and organic solvents are distributed inside the system (they are not placed inside the pores initially). Figure 2.2 shows the simulation geometry of one of the systems.

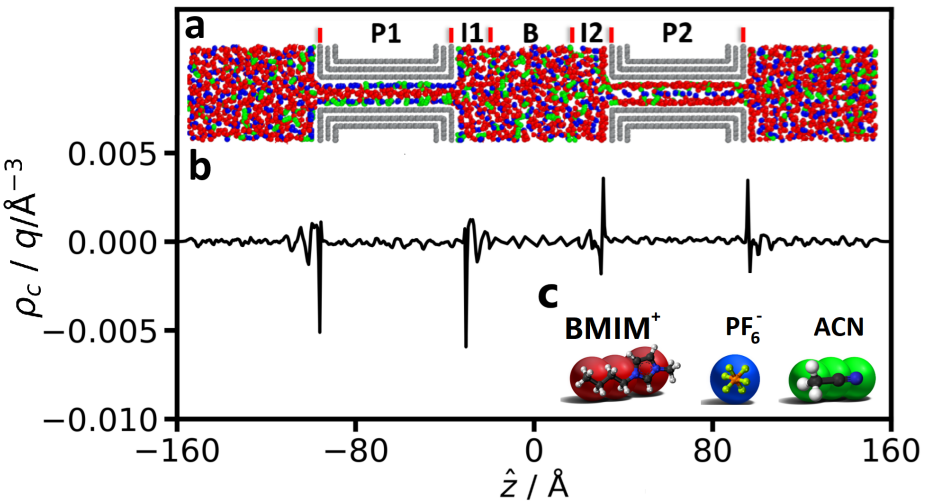

Figure 2.2. Simulated system with charged electrodes and pore size of 11.12 Å. (a) Simulation snapshot. P1 and P2 (pores), I1 and I2 (Interfaces) and B (Bulk). (b) The charge density profile along the z-axis of the above system. (c) The inset shows the coarse-grained model of ACN (green), $[BMIM^+]$ (red) and $[PF_6^-]$ (blue).

In this study, to investigate the effects of solvent dipole moment, electrode pore size, and applied voltage, 20 systems with different combinations of these parameters are established. The configurations of all system combinations are presented in Figure 2.3.

Two-dimensional periodic boundary conditions were employed in the simulations. A fixed boundary condition was applied along the direction of the electrode pores ($\hat{z}$), with invisible walls placed at both ends of the simulation box.

Simulations were performed using the LAMMPS [80] in the NVT ensemble at 400 K, with the Nosé-Hoover thermostat employed to maintain a constant temperature throughout the simulations. For each system, equilibrium simulations were run for 3.75 ns with a time step of 1.5 fs at zero electrode charge. The equilibrium data obtained was then used to initiate simulations with a constant applied voltage to the electrodes, referred to as charging simulations.

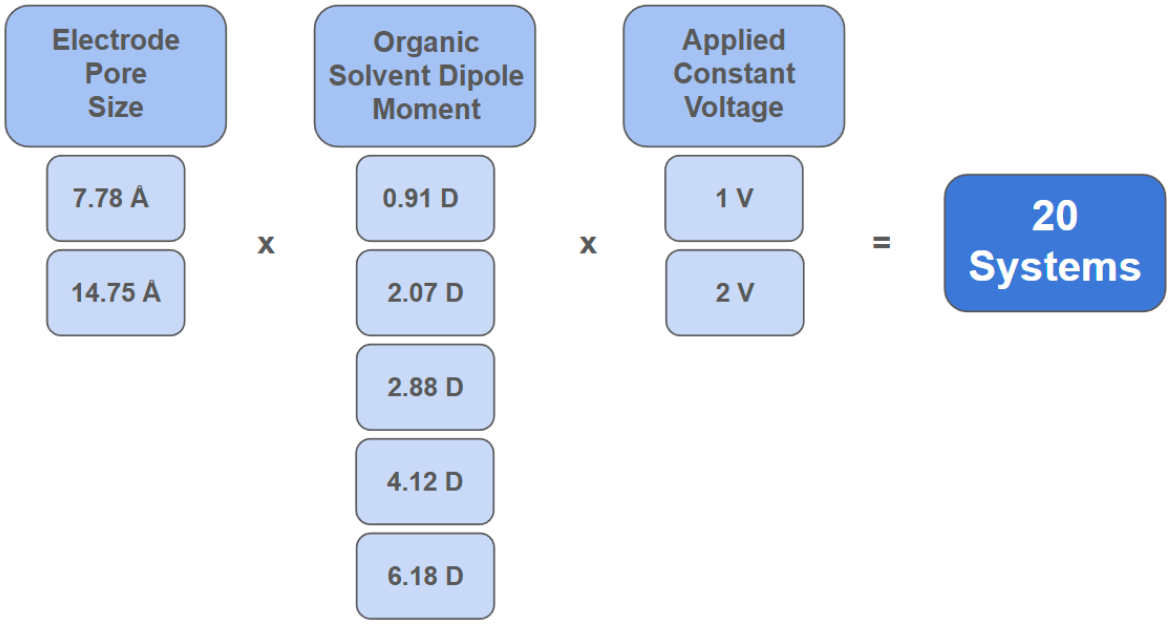

Figure 2.3. 20 different systems were designed, comprising varying combinations of 2 electrode pore sizes, 5 organic solvent dipole moments, and two applied voltages.

To allow the electrode charges to reach equilibrium, simulations of approximately 40 ns were conducted, with slight variations across different systems (±2 ns). The last 1.5 ns of the simulations were considered as the production run, and the data from this period was used to compute structural and kinetic properties under the applied potential.

2.3. Analysis Methods

After completing the simulations, several analyses were conducted to understand the kinetic and structural properties of different EDLC systems.

First, the charging profiles of the electrodes throughout the charging simulations were calculated to ensure that the system had reached its charging equilibrium and that no issues occurred during the simulations. As shown in Figure 2.2, the system contains two electrodes: one negatively charged ($\hat{z}_{\text{electrode}^-} < 0$) and the other positively charged ($\hat{z}_{\text{electrode}^+} > 0$). To calculate their charging profiles separately, the following relation

was used:

$$Q_{electrode^i} = \sum_j q_{j_{electrode^i}} \tag{2.15}$$

where $Q_{\text{electrode}^i}$ is the total charge of the positive or negative electrode, and $q_{j_{\text{electrode}^i}}$ represents the atomic charges of that electrode. Under an applied constant voltage, the charge of the supercapacitor reaches equilibrium exponentially. Therefore, the charging curve of the electrode, $Q(t)$, calculated using Equation 2.15, is fitted to an exponential model with the following equation represented as

$$Q(t) = Q_\infty(1 - e^{-\frac{t}{\tau}}) \tag{2.16}$$

where Q_∞ is infinitely equilibrated charge, τ is characteristic time of the exponential fit.

Like the verification of a smooth simulation from the electrode perspective by calculating charging profiles, the number and charge density profiles were also calculated. These calculations ensure that there are no vacuum spaces within the simulation box and provide insights into the spatial distribution of ions. The number density profile, $\rho_n(z)$, was obtained by dividing the simulation box into bins along the direction perpendicular to the electrodes ($\hat{z}$) and counting the number of particles within each bin, normalized by the bin volume. Similarly, the charge density profile, $\rho_q(z)$, was calculated by summing the charges of the particles in each bin and normalizing by the bin volume that can be expressed as:

$$\rho_n(z) = \frac{N(z)}{A\Delta z} \tag{2.17}$$

$$\rho_q(z) = \frac{Q(z)}{A\Delta z} \tag{2.18}$$

where $N(z)$ and $Q(z)$ are the number of particles and the total charge within the bin volume, A is the surface area of the bin, and Δz is the thickness of the bin along the z-axis.

By using the charge density profiles, charge density correlation lengths were calculated for the two interface regions shown in Figure 2.2 to quantify how quickly the charge density decays away from the electrode by fitting an exponential oscillatory decay function given as:

$$\rho_q(z) \propto e^{-z/l} \cos(kz + \phi) \tag{2.19}$$

where l is charge density correlation lengths, and $\cos(kz + \phi)$ is the oscillatory term with wave number k and phase shift ϕ [56].

In addition to the number and charge density profiles of the systems, free energy profiles ($\beta\Delta(z)$) were also calculated to understand the challenges electrolytes face when penetrating the pores. Free energy is calculated from the number density as follows:

$$\Delta F(z) = -k_B T \ln \rho_n(z) \tag{2.20}$$

where k_β is the Boltzmann constant and T is the temperature. From free energy profiles adsorption free energy values in electrode interface regions were calculated as:

$$\beta\Delta F_{ads}(z) = |\beta\Delta F(z_{max}) - \beta\Delta F(z_{min})| \tag{2.21}$$

To understand electrolyte dynamics separately the self-diffusion coefficients inside the positively charged pores were calculated using the Mean Square Displacement in 3-D by the following mathematical relation:

$$MSD(t) = \frac{1}{N} \sum_{i=1}^{N} |r(t) - r(t_0)|^2 \tag{2.22}$$

where $MSD(t)$ is the mean square displacement at time t, t_0 is the starting time of the calculation, N is the number of particles in the selected region and r is the position of a particle. Using the Einstein relation in equation below, diffusion coefficients were

derived from the MSDs as:

$$D = \frac{1}{6} \lim_{t \to \infty} \frac{d}{dt} \langle MSD(t) \rangle \tag{2.23}$$

where D is the self-diffusion coefficients and angle brackets denote an ensemble average where the MSD values averaged over all possible lag-times that are shorter than the length of the production data for statistically more accurate results.

As it is discussed in Section 1.2, capacitance is one of the key factors to evaluate the performance of a porous supercapacitor system and areal capacitance is calculated in this study as follows:

$$C = \frac{Q_{max}}{V_0 A} \tag{2.24}$$

where Q_{max} is positive electrode charge in equilibrium, V_0 is applied potential, and A is surface area of the electrode. For a more comprehensive grasp of capacitance, the concept of ion polarization (p_{a-c}) and effective charge separation (ξ) is introduced within the positively charged pores. To ascertain the particles contained within the pores of the positively charged electrode, a reference frame was established with a slight manipulation, wherein the origin along the z-axis of the pore was designated as z=z_{s_+}, and correspondingly, the terminus of the pore was set as z=z_{e_+}. This reference frame facilitated the identification of particles within the pore by using the following formulas:

$$p_{a-c} = \sum_{i=1}^{N_{counter}+N_{co}T} q_i \Pi\left(\frac{z_i}{|z_{s_+} - z_{e_+}|}\right) \tag{2.25}$$

$$\xi = \frac{\sum_{i=1}^{N_{counter}} \Pi\left(\frac{z_i}{|z_{s_+} - z_{e_+}|}\right)}{\sum_{i=1}^{N_{counter}} \Pi\left(\frac{z_i}{|z_{s_+} - z_{e_+}|}\right) + \sum_{i=1}^{N_{co}} \Pi\left(\frac{z_i}{|z_{s_+} - z_{e_+}|}\right)} \tag{2.26}$$

where N_{co} and $N_{counter}$ denote the counts of ions and counterions, respectively. The variable q_i signifies the charge of an ion, while Π is the rectangular function, with z_i denoting the z-coordinate of an ion.

To observe the behavior of the electrolyte inside the pores, several analyses were performed, as detailed in the Results and Discussion section. One such analysis is the spatial charge distribution of the electrolytes. In this analysis, the pore is divided into rectangular tubes along the z-axis. The dimensions of these virtual tubes are chosen as $\Delta x = 0.1\,\text{Å}$, $\Delta y = 0.1\,\text{Å}$, and $z = 60\,\text{Å}$ (the length of the pore along the z-axis). The charge density inside each tube is calculated using the production data as follows:

$$q(i) = \frac{Q(i)}{\Delta x \Delta y z} \tag{2.27}$$

where i represents the corresponding tube.

The effective dielectric constant (ϵ_{eff}) inside the positively charged electrode pore was calculated to evaluate the electrostatic environment and to further understand the effect of solvent dipole moment. The calculation involved determining the total dipole moment of the electrolyte inside the pore and its fluctuations during the production phase of the simulations. The formula for the effective dielectric constant is given as:

$$\epsilon_{\text{eff}} = 1 + \frac{3k_B TV}{4\pi} \left(\langle M^2 \rangle - \langle M \rangle^2 \right) \tag{2.28}$$

where V is the volume of the pore and $\langle M^2 \rangle - \langle M \rangle^2$ represents the total dipole moment fluctuations.

3. RESULTS AND DISCUSSION

This section presents the results and discussion of the kinetic and structural analyses of molecular dynamics (MD) simulations of EDLC systems, with a focus on the effects of pore size, applied voltage, and the dipole moment of the organic solvent. The analysis begins with the charging dynamics, where simulation data from the pre-production phase is examined to understand the charging mechanisms of different systems. This is followed by the structural dynamics, utilizing production-phase data to investigate critical features such as capacitance and the effective dielectric constant once the system reaches charging equilibrium. Finally, the behavior of the electrolyte inside the pores is analyzed, with a focus on the structure and dynamics of the electrolyte within the confined spaces of the electrode pores.

3.1. Charging Dynamics

To determine whether the systems have reached their charging equilibrium, the total charge of the electrodes must be examined. Figure 3.1 shows the total charge of the positive electrode as a function of time for four system examples. The remaining charging profiles are provided in Appendix A.1.

After a constant voltage is applied to the systems, the electrodes begin to rapidly increase their charge. Subsequently, the slope of the charging curve decreases throughout the simulation, and during the final 3–5 ns, the curves flatten, indicating that the system has reached its charging equilibrium. The simulation data beyond this point can be considered as production data.

Systems with an applied voltage of 2 V (Figure 3.1.c and d) exhibit a total equilibrium charge of approximately 15 e^-, whereas systems with an applied voltage of 1 V reach nearly half that total charge. It is also evident that, even with the same applied voltage, the equilibrium time and total charge curves are unique to each

system due to variations in pore size. Consequently, the equilibrium check and selection of production data were performed separately for each system.

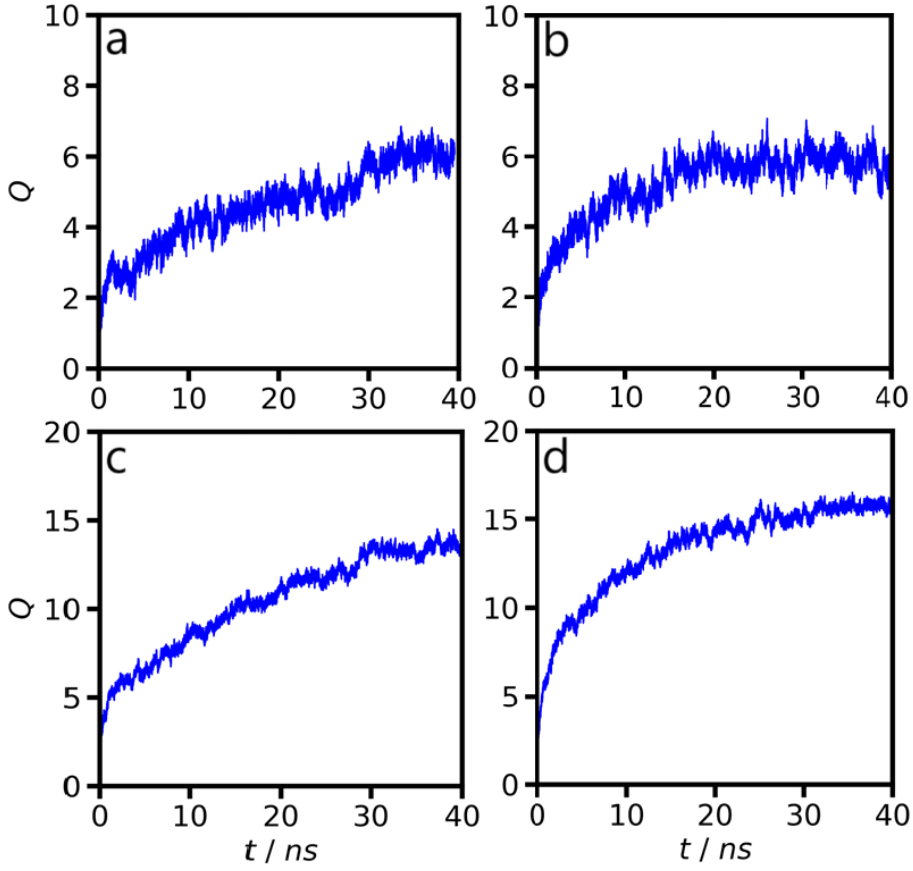

Figure 3.1. Time evolution of total charge of the positive electrodes for four different systems. (a-b) Solvent dipole moment 2.88 D, applied voltage 1 V, pore size 7.78 Å and 14.75 Å. (c-d) Solvent dipole moment 0.91 D, applied voltage 2 V, pore size 7.78 Å and 14.75 Å.

To compare the charging rates of different systems, an exponential curve was fitted to the charging profiles of the positive electrode, and the characteristic time τ (in ns) was computed using Equation 2.20. The results are presented in Figure 3.2. The observed negative correlation between τ and pore size indicates that systems with smaller pores require a longer duration to reach equilibrium. This correlation is consistent with the findings of Liu et al. [39], which demonstrated negative relationship

between pore-limiting diameter and τ due to larger diffusive barriers that hinder electrolyte penetration into smaller pores.

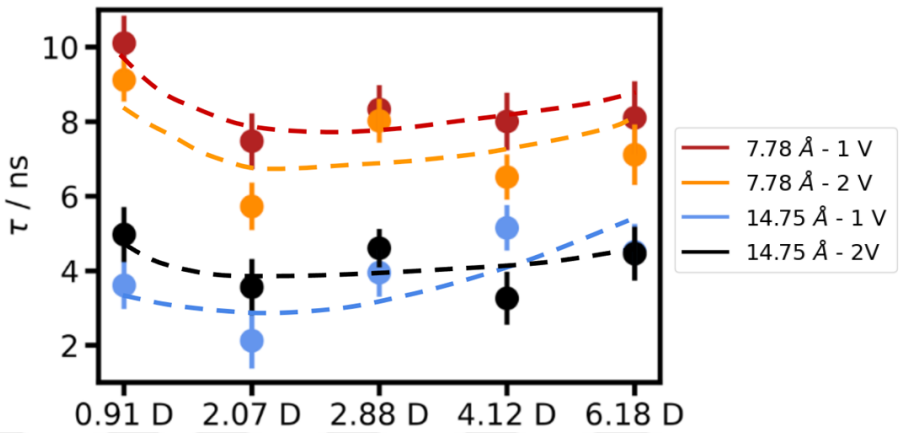

Figure 3.2. Characteristic charging time (τ) of the EDLCs as a function of dipole moments of the organic solvent.

The dipole moment also exhibits an effect on τ, with a generally positive correlation, except for systems with the lowest dipole moment and smaller pore size. At 0.91 D, systems with a pore size of 7.78 Å exhibit longer characteristic times indicating that the combination of smaller pore size and lower solvent dipole moment imposes larger diffusive barriers, making it more difficult for the electrolyte to penetrate the pore and resulting in a higher τ. For a 1 V applied voltage, this increase is 2.04 ns compared to the average τ of higher dipole moments, and for 2 V, the increase is 2.66 ns.

To understand the kinetics, ion polarization was computed over time, as shown in Figure 3.3 (Ion polarization curves for all systems is given in Appendix A.2). The rate of change in electrode charges is depicted in the ion polarization figures and represented by a color scale corresponding to the equilibrium charges. A black line, calculated as a moving average of the polarity data with a 1.5 ns window, is included to guide the eye.

When the solvent dipole moment is 0.91 D, the electrode charge begins to oscillate around its equilibrium value at approximately 24.0 ns. For a dipole moment of 2.88

D, the total charge continues to increase around 24.0 ns, and fluctuations around the equilibrium value start around 27.5 ns. When the dipole moment reaches its maximum value (6.18 D), equilibrium oscillations commence around 30.5 ns. This observation supports the conclusion drawn from the characteristic charging times: as the dipole moment increases, the time required for an EDLC system to reach equilibrium also increases.

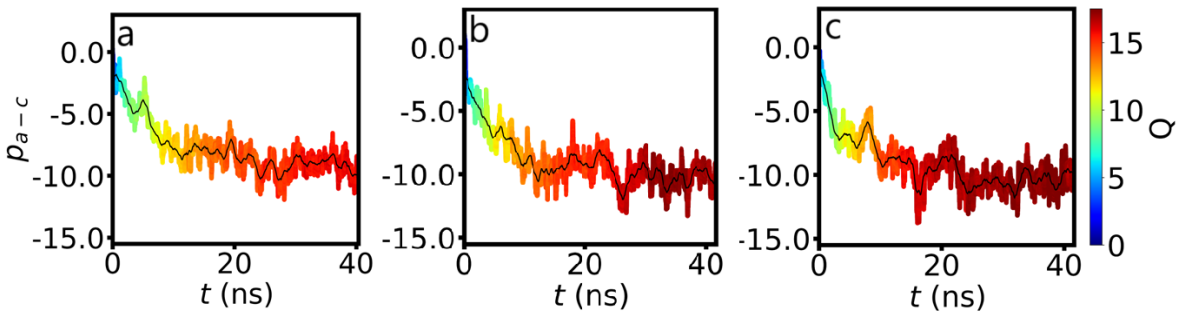

Figure 3.3. Ion polarization inside the positively charged electrodes of the systems with 14.75 Å pore and applied voltage of 2 V. (a-c) Organic solvent dipole moment is 0.91, 2.88 and 6.18 D, respectively.

From the colors of the ion polarization curves when they reach their charging equilibrium , which represent the total electrode charge, it can be observed that systems with higher solvent polarity achieve higher electrode charges. Specifically, at around 40 ns, the system with a dipole moment of 0.91 D (a) has an electrode charge of approximately 14 e^-, while the system with 2.88 D (b) reaches 16 e^-, and the system with 6.18 D (c) reaches 18.5 e^-. It is worth noting that the equilibrium charge of the electrode, and thus the capacity, is also related to the capacitance values, which will be discussed later in the capacitance analysis.

The final analysis regarding the charging dynamics of EDLC systems focuses on the self-diffusion coefficients (D_i^*) of the electrolyte inside the positively charged electrode. Figure 3.4 illustrates that the average self-diffusion coefficients follow this order: organic solvent, co-ion (cation for positively charged electrodes), and counter-ion (anion for positively charged electrodes). Organic solvent molecules is smaller

compared to others allowing for them to reach higher diffusion rates. In contrast, cations are repelled by the positively charged electrode, which facilitates their motion compared to anions. Anions are strongly attracted to the electrode surface due to electrostatic forces, which hinders their mobility and often results in their layering near the electrode and reducing their diffusion coefficients relative to the solvent.

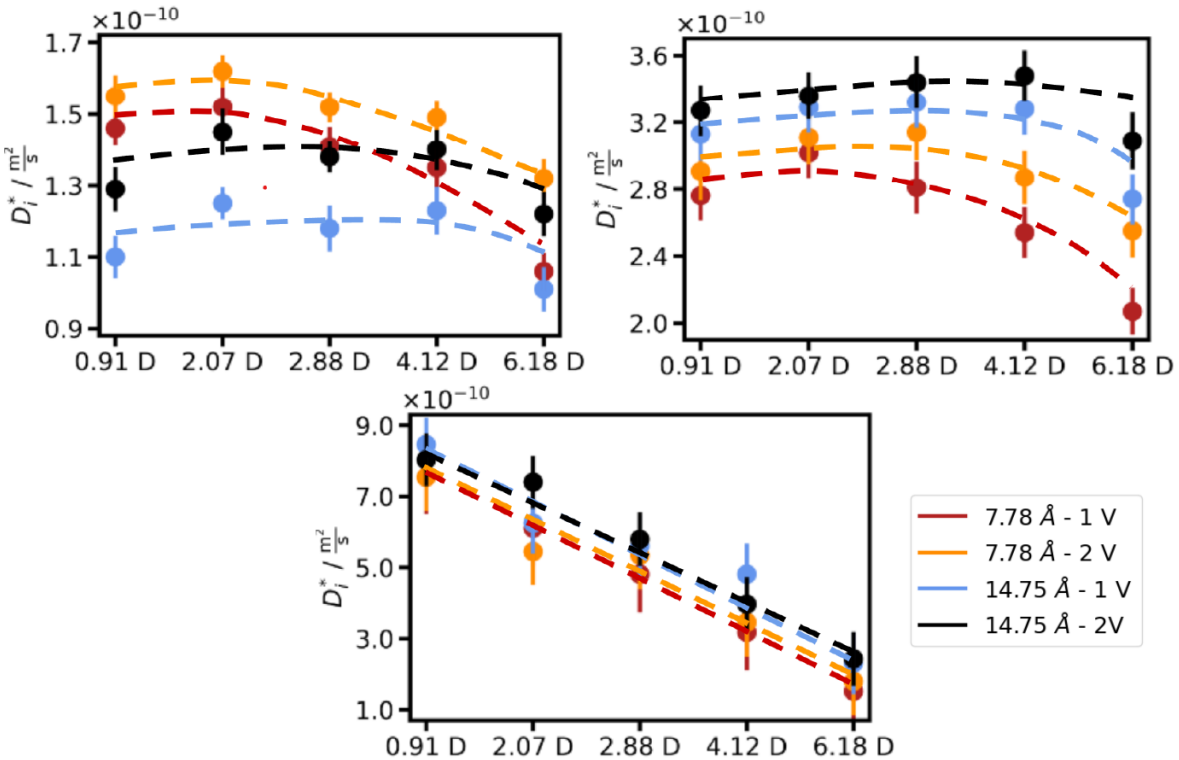

Figure 3.4. Self-Diffusion Coefficients (D_i^*) of electrolyte inside the positively charged electrodes. (a) Anion, (b) Cation and (c) Organic solvent.

Concerning anions, the applied constant voltage exhibits a positive correlation with the counter-ion's self-diffusion coefficients. Regardless of pore size and dipole moment, systems with a 2 V electrode voltage consistently show higher self-diffusion coefficients for counter-ions. Figure 3.4a illustrates that for systems with lower dipole moments ($<$ 2.88 D), those with a pore size of 7.78 Å exhibit higher self-diffusion coefficients compared to systems with larger pore sizes. For all system configurations, increasing the dipole moment from 0.91 D to 2.07 D has a positive impact of approximately 0.2 m^2/s on the self-diffusion coefficients. However, once the dipole moment

reaches 2.88 D or higher, the self-diffusion coefficients begin to decrease with increasing dipole moment. This decrease affects systems with a pore size of 7.78 Å more dramatically than those with a pore size of 14.75 Å. Consequently, the initial difference in self-diffusion coefficients between systems with a pore size of 7.78 Å and 14.75 Å at an applied voltage of 1 V and a dipole moment of 0.91 D, which is approximately 0.5 m^2/s, diminishes to zero when the dipole moment reaches its maximum value (6.18 D).

This dramatic decrease in anion self-diffusion coefficients within the positively charged electrode pores of smaller sizes, particularly for systems with solvents of higher dipole moments, can be attributed to enhanced electrostatic and confinement effects. In smaller pores, the amplified electrostatic interactions between the anions and the positively charged electrode significantly hinder ion mobility. Additionally, solvents with higher dipole moments form stronger solvation shells around anions, increasing their effective size and causing greater steric hindrance in confined geometries. The polarized solvent molecules also stabilize anion layers near the electrode surface, further restricting their motion.

For the co-ions, as shown in Figure 3.4b, a similar trend is observed with respect to the applied voltage: systems with a 2 V electrode voltage exhibit higher self-diffusion coefficients. In contrast to counter-ions, systems with a pore size of 14.75 Å consistently show higher self-diffusion coefficients for all dipole moments. This is because the electrostatic repulsion between co-ions and the electrode is reduced due to the greater distance between them, resulting in enhanced pathway availability and more efficient diffusion.

The effect of dipole moments on co-ion diffusion is similar to that observed for counter-ions. Up to a dipole moment of 2.88 D, diffusion increases across all systems. However, when the dipole moment exceeds 2.88 D, a negative correlation with diffusion is observed. For all systems, the lowest self-diffusion coefficient is reached when the dipole moment is at its maximum value of 6.18 D.

For the organic solvent, a clear and consistent trend is observed across all system configurations, regardless of pore size or electrode voltage: an increase in dipole moment leads to a nearly linear decrease in self-diffusion coefficients. This behavior can be attributed to enhanced polarization and electrostatic interactions. Solvents with higher dipole moments experience stronger alignment with the electrode's electric field, which restricts their rotational and translational freedom. A similar relationship with pore size is observed as with co-ions, where systems with a larger pore size of 14.75 Å exhibit higher self-diffusion coefficients.

In summary, for the electrolyte, self-diffusion coefficients exhibit a positive correlation with dipole moment up to a certain threshold (2.88 D). Beyond this threshold, the relationship reverses, showing a negative correlation. In contrast, for the solvent, a consistent negative correlation between dipole moment and diffusion is observed across all dipole moments.

3.2. Structural Equilibrium Dynamics

Before diving into the structural parameters that determine EDLC performance, such as capacitance and effective charge separation, it is essential to understand the simulation systems and the electrolyte distribution throughout the system. To this end, number density profiles along the z-axis are plotted for each system. These profiles serve to verify the absence of vacuum spaces or other issues within the simulation box and to provide insight into the general structure of the simulations. Figure 3.5 presents the number density profiles of anions, cations, and solvents separately, while the number density profiles for all other systems are provided in Figure A.3 and A.4.

As shown in Figure 2.2, the bulk region begins at the first minimum of the number density profile after the third peak near the negatively charged electrode interface and ends at the first minimum after the third peak near the positively charged electrode. In the figure, the dashed vertical lines represent the start and end of the electrode pores ($\hat{z} < 0$ for negatively charged pores and $\hat{z} > 0$ for positively charged pores).

The counter-ions for each electrode reach their maximum values (13.7 $Å^{-3}$ for negative electrode and 19.5 $Å^{-3}$ for the positive electrode) at the interface regions due to the attraction of opposite charges. It can also be observed that the organic solvent is distributed relatively homogeneously throughout the system.

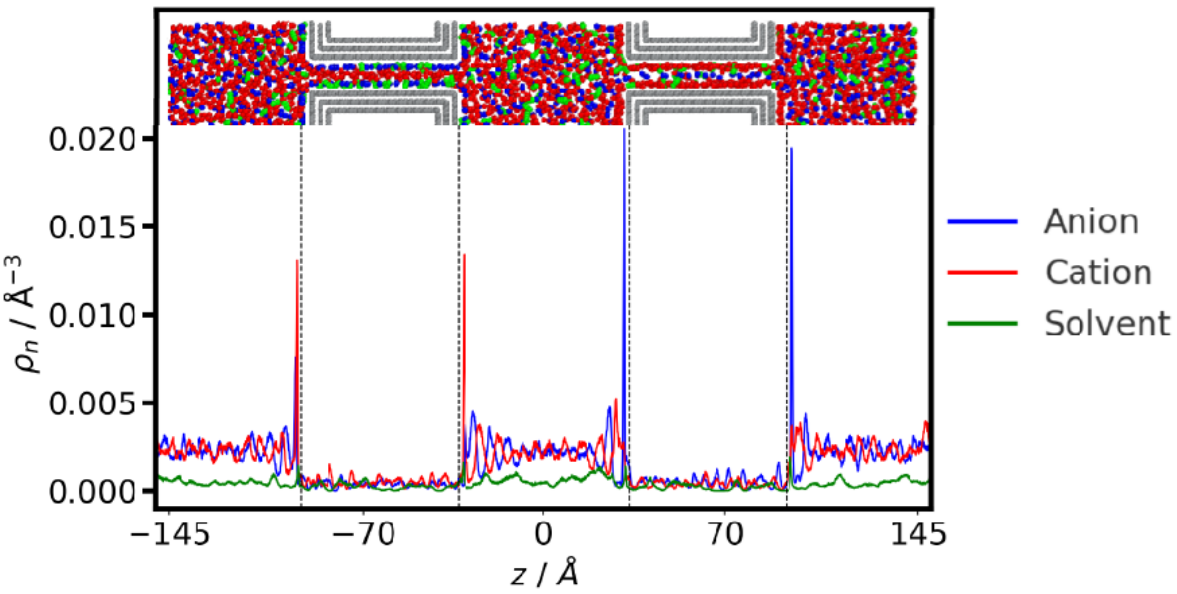

Figure 3.5. Number density profile of the EDLC system with a pore size of 7.78 Å, applied voltage of 2 V and solvent dipole moment of 0.91 D.

Parallel to the number density profiles, charge density profiles (ρ_q) are also calculated along the $\hat{z}$-axis. These profiles are used both to verify the systems for any structural issues and to calculate the charge density correlation lengths. A charge density profile of an example system is given in Figure 3.6, rest can be found in Figure A.5 and A.6.

From the charge density profile, it can be observed that within the bulk region, the total charge of the system fluctuates around 0 e^-. In the interface regions near the negative and positive electrodes, the system charge reaches its maximum and minimum, respectively. The asymmetry in the magnitude of charge density peaks near the electrode interfaces—where the maximum peak near the negatively charged electrode (0.0055 e^-) is smaller than the minimum peak near the positively charged electrode

(-0.0105 e^-) can be attributed to differences in ion dynamics and interactions. Cations, attracted to the negatively charged electrode, exhibit higher mobility with a higher self diffusion coefficient (3.4, resulting in a broader distribution and reduced peak intensity. Conversely, anions, attracted to the positively charged electrode, tend to form densely packed and structured layers, leading to a sharper and more pronounced minimum peak.

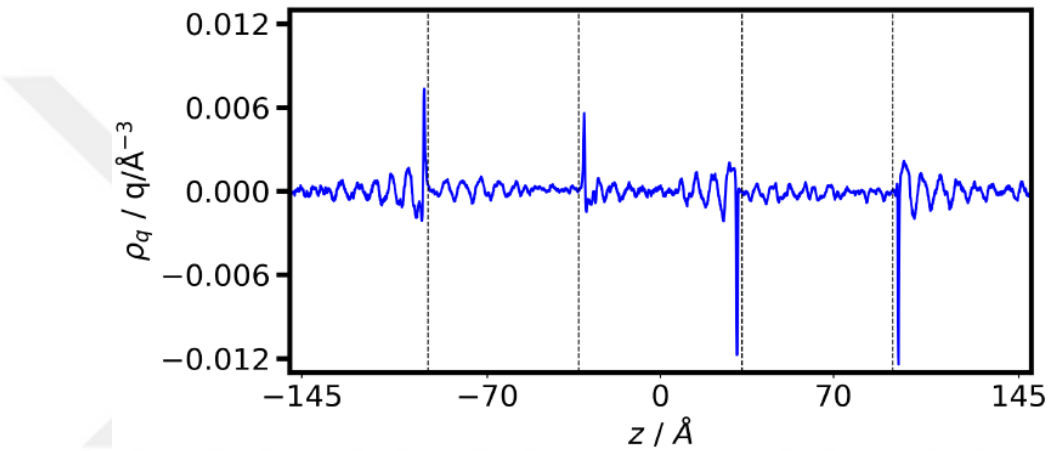

Figure 3.6. Charge density profile of the EDLC system with a pore size of 14.75 Å, applied voltage of 2 V and solvent dipole moment of 2.07 D (electrode pores are represented with the vertical dashed lines).

By fitting an exponential decay function to the charge density profiles at the two electrode interfaces, as described in Equation 2.19, the charge density correlation lengths (l) are calculated and presented in Figure 3.7. It represents the rate at which oscillations near the electrode interfaces decay into the bulk electrolyte. A higher l indicates that the electrode screens the electrolyte charges over a longer distance from its surface.

For both interfaces, the charge density correlation lengths follow the same order for nearly every system configuration: $14.75\,\text{Å} - 1\,\text{V} > 7.78\,\text{Å} - 1\,\text{V} > 14.75\,\text{Å} - 2\,\text{V} > 7.78\,\text{Å} - 2\,\text{V}$. This indicates that pore size has a positive effect on l.

The positive correlation between pore size and l can be attributed to reduced confinement effects and enhanced ion mobility in larger pores. In smaller pores, strong geometric confinement restricts ion motion and amplifies ion-ion correlations, leading to tighter ion layering and shorter l. Conversely, larger pores reduce these constraints, allowing ions and solvent molecules to diffuse more freely, resulting in more diffuse charge distributions and extended charge density correlation lengths.

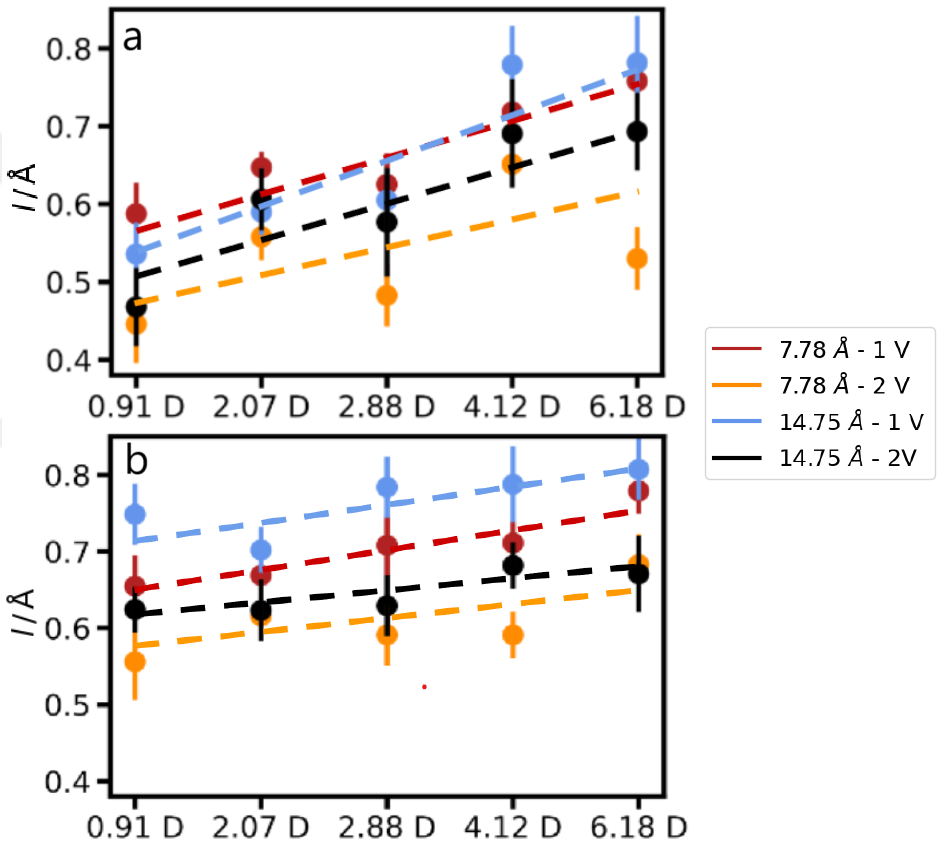

Figure 3.7. Charge density correlation lengths at the electrode interface. (a) Negatively charged electrode, (b) Positively charged electrode.

For the applied voltage, an opposite effect is observed. As the applied voltage increases, the electric field at the electrode-electrolyte interface intensifies, leading to denser ion packing near the electrode surface. This results in a faster decay of charge oscillations and, consequently, in a shorter l.

Regardless of the pore size and applied voltage combinations, all systems exhibit an increasing trend in charge density correlation length with increasing dipole moment, following an approximately linear relationship. As the dipole moment increases, solvent molecules align more strongly with the electrode's electric field, creating a more polarized environment that extends the l.

In addition to number and charge density profiles, free energy profiles ($\beta\Delta F$) were also calculated to provide insights into the energetic landscape of the systems. An example free energy profile is shown in Figure 3.8, while the free energy profiles for all systems are provided in Figure A.7 and A.8. In these profiles, local minima indicate energetically favorable regions, whereas local maxima represent energy barriers that the electrolyte must overcome to penetrate. For this study, the focus is primarily on the electrode interfaces to analyze the magnitude of the energy barriers that electrolytes must overcome to penetrate the pores.

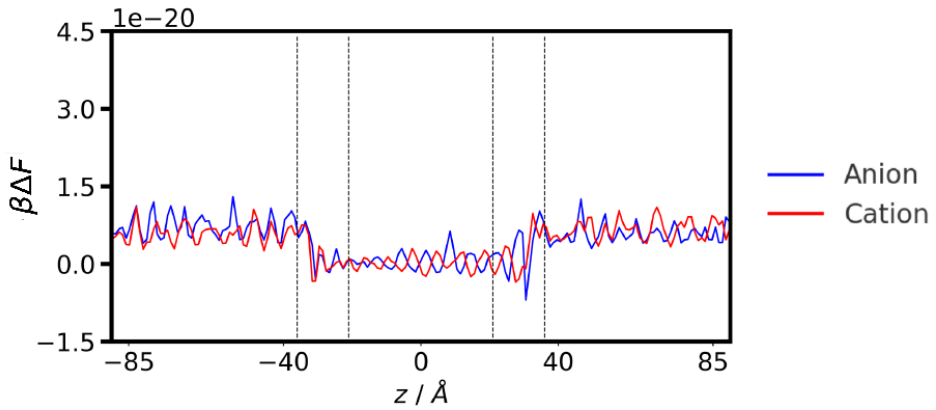

Figure 3.8. The free energy profile for the system with a 14.75 Å pore size, 2 V applied voltage, and a solvent dipole moment of 2.88 D is shown. Vertical dashed lines indicate the electrode interfaces.

From the energy profiles, the adsorption free energy for counter-ions at both electrode interfaces is calculated by subtracting the first (nearest to the electrode surface) maxima and first minima values, as described in Equation 2.21. This value quantifies the energetic favorability of ion adsorption and provides insights into the stability of

ion layers, which directly influence the EDLC structure and capacitance.

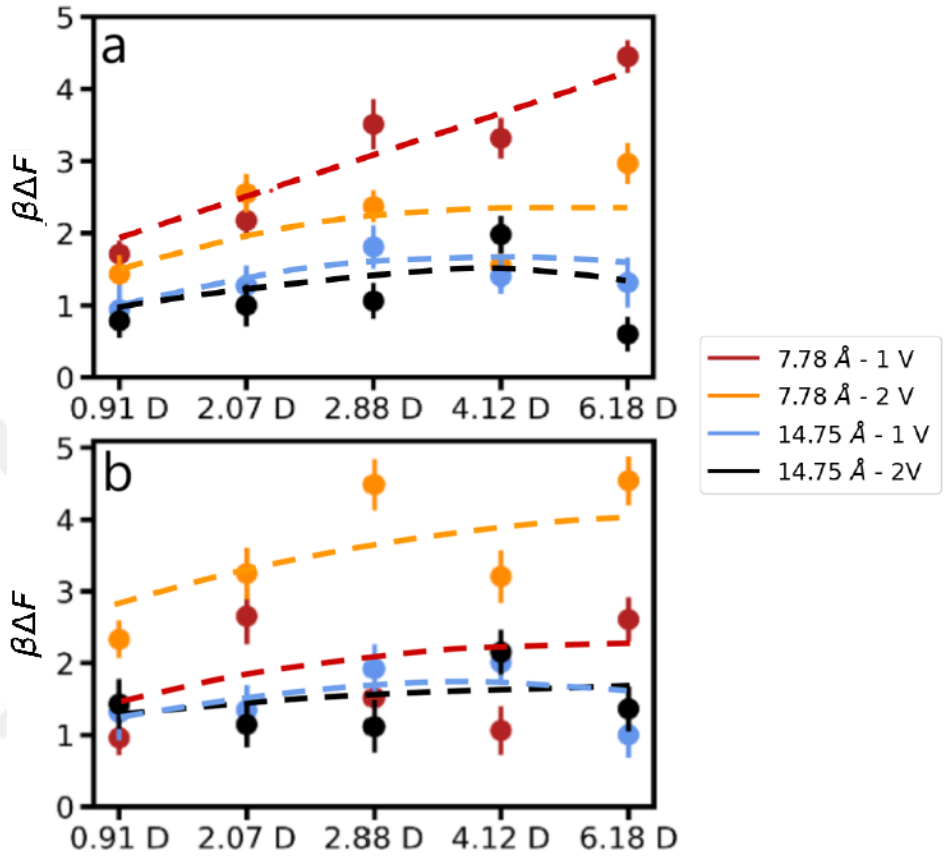

Figure 3.9. The adsorption free energy of counter-ions at the electrode interfaces: (a) Cations at negatively charged electrodes, and (b) Anions at positively charged electrodes.

As expected, for both anions and cations, the adsorption free energies are higher for systems with a 7.78 Å pore size compared to those with a 14.75 Å pore size. This is because smaller pores present greater challenges for counter-ions to penetrate. Additionally, for systems with a 1 V applied voltage, the adsorption free energies are higher compared to those with 2 V, as the electrical attraction forces between the electrode and counter-ions are weaker in the former case. Regarding the effect of dipole moment on adsorption energies, a positive correlation is observed in Figure 3.9. Notably, for systems with narrower pores, an increase in dipole moment makes it more difficult for counter-ions to enter the pore.

When the effects of pore size and dipole moment are combined, they explain the diminished impact of dipole moments in wider pores. Wider pores are inherently easier for counter-ions to enter; thus, an increase in dipole moment, which makes entry more difficult, has a less pronounced effect compared to narrower pores.

As described in the introduction chapter, one of the most critical parameters of EDLCs, determining both power and energy density (Equations 1.1 and 1.2), is capacitance. Consequently, the areal capacitance is calculated for each system and presented in Figure 3.10.

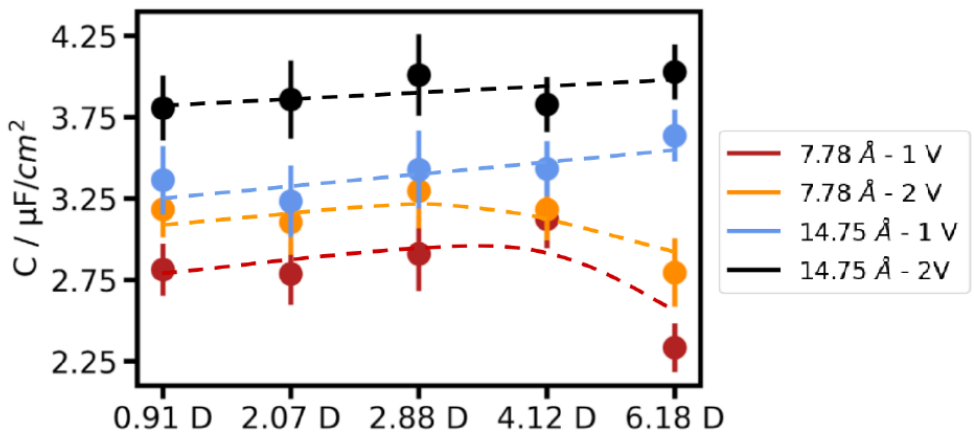

Figure 3.10. Areal Capacitance as a function of ACN dipole moment.

As shown in the figure, for both pore sizes and across all dipole moments, systems with a 2 V applied voltage exhibit higher capacitance values compared to their counterparts with a 1 V applied voltage. This difference is nearly constant across all dipole moments, amounting to approximately 0.40 ± 0.14 μF/cm^2 for 7.78 Å pores and 0.40 ± 0.18 μF/cm^2 for 14.75 Å pores. This discrepancy cannot be solely explained by the theoretical formulation. The positive correlation between applied voltage and capacitance is also influenced by the stronger electric field at the electrode-electrolyte interface, which enhances ion adsorption and charge accumulation. At higher voltages, counter-ions are drawn closer to the electrode, resulting in denser ion packing and a more compact electric double layer. Additionally, the stronger electric field reduces the

effective distance between the electrode and the charge layer, thereby increasing the capacitance.

For all systems, the influence of increasing dipole moment up to 2.88 D on capacitance is positive, consistent with findings from Jiang et al. [58]. However, in systems with a pore size exceeding the co-ion diameter of 9.79 Å, beyond the threshold of 2.88 D, the dipole moment begins to negatively impact capacitance. For both cases, the capacitance values at 6.18 D are the lowest among all dipole moments. Thus, it can be concluded that there is no direct correlation between capacitance and dipole moment; rather, there are thresholds that alter the effect of the dipole moment once exceeded.

On the other hand, systems with a pore size of 14.75 Å still exhibit a positive effect of increasing dipole moment on capacitance. However, it is worth noting that there might exist a threshold dipole moment value for 14.75 Å, similar to 7.78 Å, beyond which the capacitance values could start to decrease.

To further relate to the capacitance and gain deeper insight into the system dynamics, effective charge separation (ECS) which is an indicator of accumulated counter ions over total ions inside the pore and effective dielectric constants (EDC) were calculated and are presented in Figure 3.11, based on Equations 2.26 and 2.28, respectively.

From Figure 3.11, similar trends to those observed for capacitance can be noted. As with capacitance, the order of effective charge separation (ECS) for applied voltage is: $2\,\mathrm{V} > 1\,\mathrm{V}$. However, in the case of ECS, systems with wider pores do not always exhibit higher ECS values.

A positive correlation between dipole moment and ECS is also observed in all systems with an organic solvent that has a dipole moment of 2.88 D or lower. For systems with a pore size of 14.75 Å, this increase persists across all dipole moments. In contrast, for systems with a pore size of 7.78 Å, the positive trend in ECS reverses when the dipole moment reaches 6.18 D, similar to the behavior observed for capacitance.

For the effective dielectric constant (EDC) shown in Figure 3.11.b, in terms of the order of magnitude for both EDC and capacitance, the systems follow the order: $14.75\,\text{Å} - 2\,\text{V} > 14.75\,\text{Å} - 1\,\text{V} > 7.78\,\text{Å} - 2\,\text{V} > 7.78\,\text{Å} - 1\,\text{V}$.

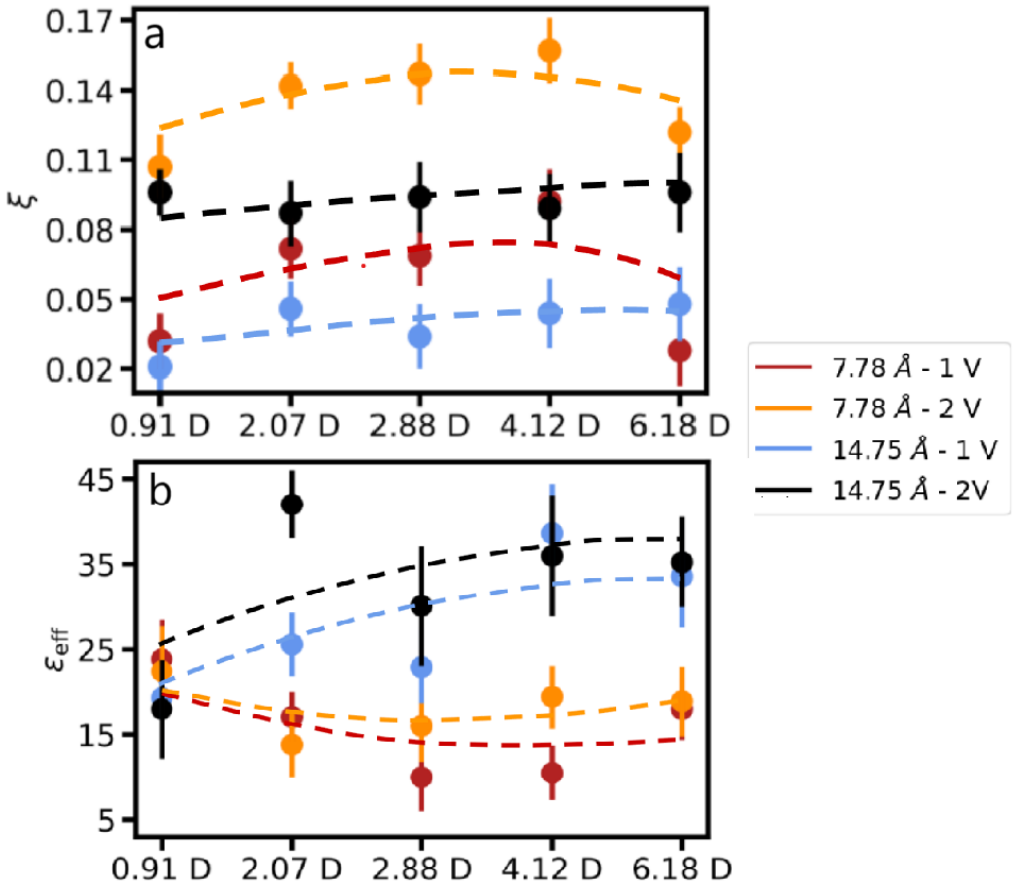

Figure 3.11. (a) Effective charge separation ξ and (b) Effective dielectric constant ϵ_{eff}

For systems with a pore size of 14.75 Å, both capacitance and EDC increase with increasing dipole moment. For capacitance, the increase with dipole moment is nearly linear for both applied voltage, with ranges from $3.24 \pm 0.21 \mu F/cm^2$ to $3.62 \pm 0.24 \mu F/cm^2$ for 1 V and $3.76 \pm 0.24 \mu F/cm^2$ to $3.91 \pm 0.25 \mu F/cm^2$ for 2 V.

In contrast, for systems with a pore size of 7.78 Å, the capacitance and EDC values do not exhibit the same trend as the dipole moment increases. For capacitance, the dipole moment has a positive effect up to 2.88 D, after which this effect reverses, and capacitance begins to decrease with further increases in dipole moment. However,

for EDC, the opposite trend is observed, as shown in Figure 3.11.b. EDC decreases until 2.88 D and then begins to increase slightly beyond this threshold.

3.3. Electrolyte Behaviors Inside the Pores

For the final part of the results and discussion chapter, the focus shifts to the regions inside the pores. The distribution of electrolytes along the y-axis of the pores is examined more closely to establish a connection with the structural dynamics of EDLCs. To achieve this, a spatial charge heat map is calculated, alongside with the center-of-mass position distribution and charge distribution along the y-axis of the electrolyte inside the positively charged electrodes. These analyses are illustrated in Figures 3.12 and 3.13.

In the system with a pore size of 7.78 Å, the spatial distribution of electrolyte particles shows alignment near the electrode walls. In Figure 3.12, this phenomenon is evident in the central segment of the curves, where the values approach zero for co-ions, counter-ions, and organic solvents. When the pore size increases to 14.75 Å, both co-ions and counter-ions begin to disperse toward the central region of the pore. This behavior is illustrated in Figure 3.13. The newly formed co-ion layer in the middle of the pore also influences the charging dynamics, as proposed by Feng et al. [36]. As shown in Figure 3.10, the introduction of this alternating co-ion layer leads to an enhanced capacitance compared to systems lacking a counterion layer, which is positioned midway between the two slit walls.

Another difference between the systems with two different pore sizes is the magnitude of the number density for the electrolyte in the nearest layer to the electrode. For the co-ions in the 7.78 Å systems, the number density values for the electrolyte layers are approximately 0.012 $Å^{-3}$, which is nearly the same as in the 14.75 Å systems. However, for the counter-ions, there is a substantial difference between the two pore sizes. While systems with a pore size of 7.78 Å exhibit a counter-ion number density of 0.018 $Å^{-3}$, this value increases to 0.022 $Å^{-3}$. Considering a higher increase in ca-

pacitance with larger pore sizes, it can be concluded that the increase in counter-ion numbers in the electrolyte layer at the electrode interface inside the pores has a direct correlation with the performance of the EDLC.

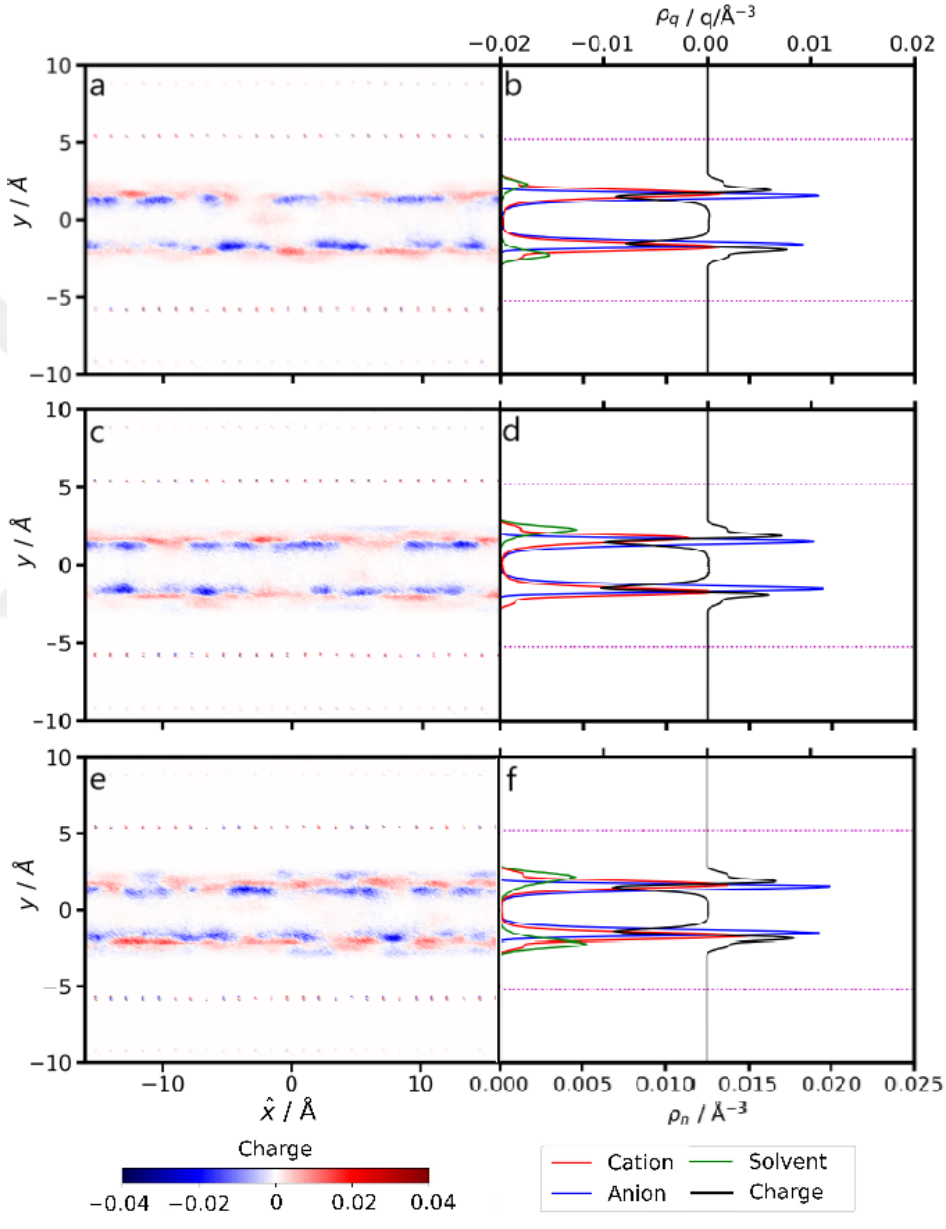

Figure 3.12. (a-c-e) Spatial charge distribution heatmaps and (b-d-f) electrolyte number density profiles inside the positively charged electrode of systems with a pore size of 7.78 Å, applied voltage of 1V and dipole moments of (a-b) 0.91 D, (c-d) 2.88 D, and (e-f) 6.18 D.

For the effect of dipole moment, the same argument made for the effect of pore size appears valid. In Figure 3.10, it is observed that capacitance and dipole moment have a positive relationship for all dipole moments in systems with a 14.75 Å pore size.

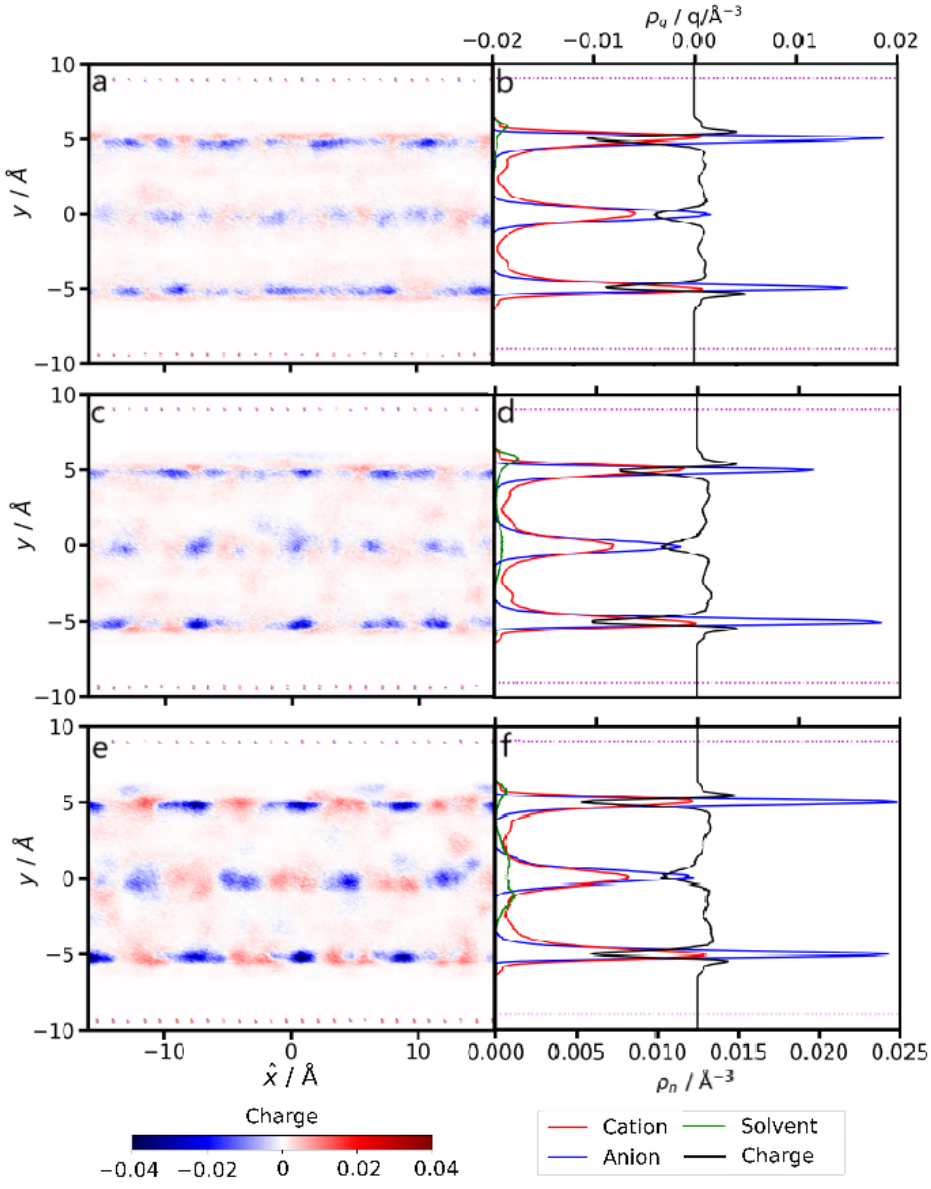

Figure 3.13. (a-c-e) Spatial charge distribution heatmaps and (b-d-f) electrolyte number density profiles inside the positively charged electrode of systems with a pore size of 14.75 Å, applied voltage of 1V and dipole moments of (a-b) 0.91 D, (c-d) 2.88 D, and (e-f) 6.18 D.

For the systems depicted in Figure 3.13, the capacitance values are 3.30 ± 0.24 μF/cm^2, 3.37 ± 0.22 μF/cm^2, and 3.64 ± 0.18 μF/cm^2. The average total charge for the electrolyte layers nearest to the electrode in Figures 3.13a, 3.13d, and 3.13f are -0.095 q/Å^3, -0.098 q/Å^3, and -0.104 q/Å^3, respectively, for the same systems.

On the other hand, for the smaller pore size of 7.78 Å, the positive correlation between capacitance and dipole moment is not observed at higher dipole moments of 4.12 D and 6.18 D. The capacitance values of the systems depicted in Figure 3.12 are 2.78 ± 0.14 μF/cm^2, 2.80 ± 0.16 μF/cm^2, and 2.32 ± 0.12 μF/cm^2. The charge densities of the electrolyte layer inside the pore are 0.085 q/Å^3, 0.086 q/Å^3, and 0.073 q/Å^3. These changes are closely aligned with the observed trends in capacitance.

4. CONCLUSION AND RECOMMENDATIONS

The demand for energy in the modern world is growing rapidly due to increasing population and humanity's dependence on electricity. As a result, advancements in energy storage and generation methods with higher energy and power densities are becoming increasingly critical. In this context, supercapacitors, commonly referred to as Electrical Double-Layer Capacitors (EDLCs), represent one of the most promising innovations, gaining significant attention in both academic and industrial fields. Since this area of research is relatively new, there is substantial potential for improvement, both theoretically and experimentally.

To explore this concept, this study focuses on the kinetics and structural dynamics of EDLCs using molecular dynamics (MD) simulations. The parameters varied in the simulations include pore size, applied voltage, and solvent dipole moment. These factors are critical in determining EDLC performance and efficiency. MD simulations were conducted for twenty distinct system configurations, incorporating two pore sizes (7.78 Å and 14.75 Å), five organic solvent dipole moments (0.91 D, 2.07 D, 2.88 D, 4.12 D, and 6.18 D), and two applied voltages (1 V and 2 V). The simulations were performed for an average total duration of 40 ns with a time step of 1.5 fs at a temperature of 400 K. The last 1.5 ns of data was used as the production data, where all equilibrium analyses were conducted.

The findings highlight several key aspects of EDLC behavior. Charging dynamics reveal that the pore with 7.48 Å pore size exhibit longer equilibrium times due to larger diffusive barriers, consistent with prior studies. The characteristic charging time, τ, shows a positive correlation with dipole moment, except at the lowest dipole moment in systems with narrow pores. Higher applied voltages accelerate the charging process and result in greater equilibrium charges, enhancing the energy storage capability.

The structural equilibrium dynamics of EDLCs demonstrate successful creation of bulk regions in all systems, with peak ion concentrations near electrode interfaces. charge density correlation lengths (l) increase with pore size and dipole moment. Enhanced solvent polarization near the electrodes extends the electric field deeper into the electrolyte, further influencing performance.

One of the key factors for an EDLC system is capacitance, as it is a primary determinant of the energy and power density of a supercapacitor. The areal capacitance for different systems indicates that wider pores and higher applied voltages positively impact capacitance across all configurations. For any given solvent dipole moment, a narrower pore or a lower applied electrode voltage cannot surpass its counterpart in terms of capacitance.

The effect of changing dipole moment yields one of the most intriguing findings of this study. For systems with a pore size of 14.75 Å, there is a positive correlation between dipole moment and capacitance across all dipole moment values. In contrast, for the narrower pore size (7.78 Å), the relationship between dipole moment and capacitance is less straightforward. Up to a threshold dipole moment of 2.88 D, capacitance increases with dipole moment, following a trend similar to that observed in wider pores. However, beyond this threshold, capacitance begins to decrease, reaching its lowest value for the system when the dipole moment is at its maximum (6.18 D). This negative effect is attributed to highly polarized solvent molecules, which lead to the exclusion of ions from the pores. Thus, it can be concluded that there is no direct correlation between capacitance and dipole moment; rather, thresholds exist that alter the effect of dipole moment once exceeded. Capacitance values also exhibit a direct correlation with effective dielectric constants, with wider pores and higher voltages generally achieving higher values. However, nonlinear trends with dipole moments highlight the complex dependencies on structural and electrostatic factors. Therefore, the non-monotonic behavior of capacitance with dipole moment underscores the importance of optimizing solvent polarity to maximize EDLC performance.

After investigating the general structural properties of the system, the focus shifts to the electrolyte behavior within the pores. Spatial charge analysis, combined with the number density of the electrolyte inside the pores, reveals that systems with wider pores (14.75 Å) exhibit a more uniform ion distribution, with additional co-ion layers forming in the pore centers. Furthermore, the number density of layers near the electrode shows trends that are closely aligned with changes in capacitance.

For the next part, several recommendations for future research and development are proposed to enhance EDLC design and performance. First, optimizing pore sizes is critical. In this study, although the largest pore size demonstrated the best performance, only two pore size options were examined. Expanding this range (especially between 10 Å and 14 Å) will provide deeper insights into the effect of pore size on supercapacitors.

Second, solvent selection and modifications play a vital role, as described in the previous paragraphs. Future studies should explore the combination of solvent and pore size that yields the highest performance. Solvent mixtures, combining ionic liquids and organic solvents, could also be investigated to achieve favorable viscosities and dielectric properties.

Higher voltage stability is another area of interest. Applying voltages higher than 2 V could enhance energy storage but would require the development of electrolytes with improved electrochemical stability. Electrolytes containing ionic liquids with tailored anion-cation combinations may provide both stability and enhanced capacitance.

More broadly, future simulation studies should expand the parameter space, such as varying ion concentrations and exploring multi-component electrolytes, to gain deeper insights into real-world EDLC performance. Coupling MD simulations with machine learning models could also expedite the identification of optimal system configurations.

In conclusion, this thesis contributes to the growing understanding of EDLC dynamics, providing actionable insights for both MD simulation and the physical design of supercapacitors. By addressing the identified challenges, future research and development efforts can further optimize EDLC performance for diverse applications in energy storage.

REFERENCES

1. Chu, S., "Opportunities and Challenges for a Sustainable Energy Future", *Nature*, Vol. 488, No. 7411, pp. 294–303, 2012.

2. Kubota, K., M. Dahbi, T. Hosaka, S. Kumakura and S. Komaba, "Towards K-Ion and Na-Ion Batteries as Beyond Li-Ion", *The Chemical Record*, Vol. 18, No. 4, pp. 459–479, 2018.

3. Kim, B. K., S. Sy, A. Yu and J. Zhang, *Electrochemical Supercapacitors for Energy Storage and Conversion*, pp. 1–25, John Wiley Sons, Ltd, 2015.

4. Burke, A., "RD Considerations for the Performance and Application of Electrochemical Capacitors", *Electrochimica Acta*, Vol. 53, No. 3, pp. 1083–1091, 2007.

5. Pershaanaa, M., S. Bashir, S. Ramesh and K. Ramesh, "Every Bite of Supercap: A Brief Review on Construction and Enhancement of Supercapacitor", *Journal of Energy Storage*, Vol. 50, p. 104599, 2022.

6. Miller, J. and P. Simon, "Materials Science—Electrochemical Capacitors for Energy Management", *Science*, Vol. 321, No. 5889, pp. 651–2, 2008.

7. Karthikeyan, S., B. Narenthiran, A. Sivanantham, L. D. Bhatlu and T. Maridurai, "Supercapacitor: Evolution and Review", *Materials Today: Proceedings*, Vol. 46, pp. 3984–3988, 2021.

8. Wu, D., X. Xie, Y. Ma, J. Zhang, C. Hou, X. Sun, X. Yang, Y. Zhang, H. Kimura and W. Du, "Morphology Controlled Hierarchical NiS/Carbon Hexahedrons Derived From Nitrilotriacetic Acid-Assembly Strategy For High-Performance Hybrid Supercapacitors", *Chemical Engineering Journal*, Vol. 433, p. 133673, 2022.

9. Ma, Y., X. Xie, W. Yang, Z. Yu, X. Sun, Y. Zhang, X. Yang, H. Kimura, C. Hou,

Z. Guo and W. Du, "Recent Advances in Transition Metal Oxides With Different Dimensions as Electrodes for High-Performance Supercapacitors", *Advanced Composites and Hybrid Materials*, Vol. 4, No. 4, p. 906–924, 2021.

10. Du, W., X. Wang, J. Zhan, X. Sun, L. Kang, F. Jiang, X. Zhang, Q. Shao, M. Dong, H. Liu, V. Murugadoss and Z. Guo, "Biological Cell Template Synthesis of Nitrogen-Doped Porous Hollow Carbon Spheres/MnO2 Composites for High-Performance Asymmetric Supercapacitors", *Electrochimica Acta*, Vol. 296, pp. 907–915, 2019.

11. Cossutta, M., V. Vretenar, T. A. Centeno, P. Kotrusz, J. McKechnie and S. J. Pickering, "A Comparative Life Cycle Assessment of Graphene and Activated Carbon in a Supercapacitor Application", *Journal of Cleaner Production*, Vol. 242, p. 118468, 2020.

12. Cheng, F., X. Yang, S. Zhang and W. Lu, "Boosting the Supercapacitor Performances of Activated Carbon With Carbon Nanomaterials", *Journal of Power Sources*, Vol. 450, p. 227678, 2020.

13. Adusei, P. K., S. Gbordzoe, S. N. Kanakaraj, Y.-Y. Hsieh, N. T. Alvarez, Y. Fang, K. Johnson, C. McConnell and V. Shanov, "Fabrication and Study of Supercapacitor Electrodes Based on Oxygen Plasma Functionalized Carbon Nanotube Fibers", *Journal of Energy Chemistry*, Vol. 40, pp. 120–131, 2020.

14. Balaji, S. S., M. Karnan, P. Anandhaganesh, S. M. Tauquir and M. Sathish, "Performance Evaluation of B-Doped Graphene Prepared Via Two Different Methods in Symmetric Supercapacitor Using Various Electrolytes", *Applied Surface Science*, Vol. 491, pp. 560–569, 2019.

15. E, L., W. Li, C. Ma, Z. Xu and S. Liu, "CO2-Activated Porous Self-Templated N-Doped Carbon Aerogel Derived From Banana for High-Performance Supercapacitors", *Applied Surface Science*, Vol. 457, pp. 477–486, 2018.

16. Peng, H., B. Yao, X. Wei, T. Liu, T. Kou, P. Xiao, Y. Zhang and Y. Li, "Pore and Heteroatom Engineered Carbon Foams for Supercapacitors", *Advanced Energy Materials*, Vol. 9, No. 19, p. 1803665, 2019.

17. Malmberg, S., M. Arulepp, N. Savest, E. Tarasova, V. Vassiljeva, I. Krasnou, M. Käärik, V. Mikli and A. Krumme, "Directly Electrospun Electrodes for Electrical Double-Layer Capacitors From Carbide-Derived Carbon", *Journal of Electrostatics*, Vol. 103, p. 103396, 2020.

18. Krüner, B., C. Odenwald, A. Quade, G. Kickelbick and V. Presser, "Influence of Nitrogen-Doping for Carbide-Derived Carbons on the Supercapacitor Performance in an Organic Electrolyte and an Ionic Liquid", *Batteries Supercaps*, Vol. 1, No. 4, pp. 135–148, 2018.

19. Cherusseri, J. and K. K. Kar, "Hierarchically Mesoporous Carbon Nanopetal Based Electrodes for Flexible Supercapacitors With Super-Long Cyclic Stability", *Journal of Materials Chemistry A*, Vol. 3, No. 43, pp. 21586–21598, 2015.

20. Panja, T., D. Bhattacharjya and J.-S. Yu, "Nitrogen and Phosphorus Co-Doped Cubic Ordered Mesoporous Carbon as a Supercapacitor Electrode Material With Extraordinary Cyclic Stability", *Journal of Materials Chemistry A*, Vol. 3, No. 35, pp. 18001–18009, 2015.

21. Liu, C., Z. Yu, D. Neff, A. Zhamu and B. Z. Jang, "Graphene-Based Supercapacitor With an Ultrahigh Energy Density", *Nano Letters*, Vol. 10, No. 12, pp. 4863–4868, 2010.

22. Wong, S. I., J. Sunarso, B. T. Wong, H. Lin, A. Yu and B. Jia, "Towards Enhanced Energy Density of Graphene-Based Supercapacitors: Current Status, Approaches, and Future Directions", *Journal of Power Sources*, Vol. 396, pp. 182–206, 2018.

23. Karthika, P., "Functionalized Exfoliated Graphene Oxide as Supercapacitor Elec-

trodes", *Soft Nanoscience Letters*, Vol. 2, No. 4, pp. 59–66, 2012.

24. Kim, T. Y., H. W. Lee, M. Stoller, D. R. Dreyer, C. W. Bielawski, R. S. Ruoff and K. S. Suh, "High-Performance Supercapacitors Based on Poly(Ionic Liquid)-Modified Graphene Electrodes", *ACS Nano*, Vol. 5, No. 1, pp. 436–442, 2011.

25. Zhang, L. L., R. Zhou and X. Zhao, "Graphene-Based Materials as Supercapacitor Electrodes", *Journal of Materials Chemistry*, Vol. 20, No. 29, pp. 5983–5992, 2010.

26. Balasubramaniam, S., A. Mohanty, S. K. Balasingam, S. Kim and A. Ramadoss, "Comprehensive Insight Into the Mechanism, Material Selection and Performance Evaluation of Supercapatteries", *Nano-Micro Letters*, Vol. 12, No. 85, 2020.

27. Simon, P., Y. Gogotsi and B. Dunn, "Where do batteries end and supercapacitors begin?", , 2014.

28. Lee, J., J. Kim and T. Hyeon, "Recent Progress in the Synthesis of Porous Carbon Materials", *Advanced Materials*, Vol. 18, No. 16, pp. 2073–2094, 2006.

29. Frackowiak, E., "Carbon Materials for Supercapacitor Application", *Physical Chemistry Chemical Physics*, Vol. 9, No. 15, pp. 1774–1785, 2007.

30. Zhang, L. L. and X. S. Zhao, "Carbon-Based Materials as Supercapacitor Electrodes", *Chemical Society Reviews*, Vol. 38, No. 9, pp. 2520–2531, 2009.

31. Liu, T., F. Zhang, Y. Song and Y. Li, "Revitalizing Carbon Supercapacitor Electrodes With Hierarchical Porous Structures", *Journal of Materials Chemistry A*, Vol. 5, No. 34, pp. 17705–17733, 2017.

32. Ratajczak, P., M. E. Suss, F. Kaasik and F. Béguin, "Carbon Electrodes for Capacitive Technologies", *Energy Storage Materials*, Vol. 16, pp. 126–145, 2019.

33. Kondrat, S., N. Georgi, M. V. Fedorov and A. A. Kornyshev, "A Superionic State in Nanoporous Double-Layer Capacitors: Insights From Monte Carlo Simulations", Vol. 13, pp. 11359–11366, 2011.

34. Frackowiak, E., G. Lota, J. Machnikowski, C. Vix-Guterl and F. Béguin, "Optimisation of Supercapacitors Using Carbons With Controlled Nanotexture and Nitrogen Content", Vol. 51, pp. 2209–2214, 2006.

35. Jiang, D. E., Z. Jin, D. Henderson and J. Wu, "Solvent Effect on the Pore-Size Dependence of an Organic Electrolyte Supercapacitor", *Journal of Physical Chemistry Letters*, Vol. 3, No. 13, pp. 1727–1731, 2012.

36. Feng, G. and P. T. Cummings, "Supercapacitor Capacitance Exhibits Oscillatory Behavior as a Function of Nanopore Size", *Journal of Physical Chemistry Letters*, Vol. 2, No. 22, pp. 2859–2864, 2011.

37. Kondrat, S., C. Pérez, V. Presser, Y. Gogotsi and A. Kornyshev, "Effect of Pore Size and Its Dispersity on the Energy Storage in Nanoporous Supercapacitors", *Energy Environmental Science*, Vol. 5, pp. 6474–6479, 2012.

38. Péan, C., C. Merlet, B. Rotenberg, P. A. Madden, P. L. Taberna, B. Daffos, M. Salanne and P. Simon, "On the Dynamics of Charging in Nanoporous Carbon-Based Supercapacitors", *ACS Nano*, Vol. 8, No. 2, pp. 1576–1583, 2014.

39. Liu, Y. M., C. Merlet and B. Smit, "Carbons With Regular Pore Geometry Yield Fundamental Insights Into Supercapacitor Charge Storage", *ACS Central Science*, Vol. 5, No. 11, pp. 1813–1823, 2019.

40. Korkut, A. S. and B. Uralcan, "Reduced Graphene Oxide/Ionic Liquid Composites With Tunable Interlayer Spacing for Improved Charge/Discharge Kinetics in Supercapacitors", *Nanotechnology*, Vol. 34, No. 23, p. 235402, 2023.

41. McDaniel, J. G., "Capacitance of Carbon Nanotube/Graphene Composite Elec-

trodes With [BMIM+][BF4]/Acetonitrile: Fixed Voltage Molecular Dynamics Simulations", *Journal of Physical Chemistry C*, Vol. 126, No. 13, pp. 5822–5837, 2022.

42. Suo, L., O. Borodin, T. Gao, M. Olguin, J. Ho, X. Fan, C. Luo, C. Wang and K. Xu, "Water-in-Salt Electrolyte Enables High-Voltage Aqueous Lithium-Ion Chemistries", *Science*, Vol. 350, No. 6263, pp. 938–943, 2015.

43. Forse, A. C., J. M. Griffin, C. Merlet, J. Carretero-Gonzalez, A. R. O. Raji, N. M. Trease and C. P. Grey, "Direct observation of ion dynamics in supercapacitor electrodes using in situ diffusion NMR spectroscopy", *Nature Energy*, Vol. 2, No. 3, 2017.

44. Tu, Y.-J., S.-C. Wu and J. G. McDaniel, "Importance of Anion-Anion Pairing for Capacitance of Carbon/Ionic Liquid Interfaces", *Journal of Physical Chemistry C*, Vol. 2022, No. 46, pp. 20213–20225, 2021.

45. Yoon, H., P. Howlett, A. Best, M. Forsyth and D. MacFarlane, "Fast Charge/Discharge of Li Metal Batteries Using an Ionic Liquid Electrolyte", *Journal of The Electrochemical Society*, Vol. 160, No. 10, pp. A1629–A1637, 2013.

46. Lin, R., P. Huang, J. Segalini, C. Largeot, P. L. Taberna, J. Chmiola, Y. Gogotsi and P. Simon, "Solvent Effect on the Ion Adsorption From Ionic Liquid Electrolyte Into Sub-Nanometer Carbon Pores", *Electrochimica Acta*, Vol. 54, No. 27, p. 7025, 2009.

47. Pivnic, K., F. Bresme, A. A. Kornyshev and M. Urbakh, "Structural Forces in Mixtures of Ionic Liquids With Organic Solvents", *Langmuir*, Vol. 35, No. 47, pp. 15410–15420, 2019.

48. Merlet, C., M. Salanne, B. Rotenberg and P. A. Madden, "Influence of Solvation on the Structural and Capacitive Properties of Electrical Double-Layer Capaci-

tors", *Electrochimica Acta*, Vol. 101, pp. 262–271, 2013.

49. Su, H., C. Lian, J. Liu and H. Liu, "Machine Learning Models for Solvent Effects on Electric Double-Layer Capacitance", *Chemical Engineering Science*, Vol. 202, pp. 186–193, 2019.

50. Liu, K. and J. Wu, "Boosting the Performance of Ionic-Liquid-Based Supercapacitors With Polar Additives", *Journal of Physical Chemistry C*, Vol. 120, No. 42, pp. 24041–24047, 2016.

51. Chaban, V. V., I. V. Voroshylova, O. N. Kalugin and O. V. Prezhdo, "Acetonitrile Boosts Conductivity of Imidazolium Ionic Liquids", *Journal of Physical Chemistry B*, Vol. 116, No. 26, pp. 7719–7727, 2012.

52. Shim, Y., H. J. Kim and Y. Jung, "Graphene-Based Supercapacitors in the Parallel-Plate Electrode Configuration: Ionic Liquids Versus Organic Electrolytes", *Faraday Discussions*, Vol. 154, pp. 249–263, 2012.

53. Burt, R., K. Breitsprecher, B. Daffos, P.-L. Taberna, P. Simon, G. Birkett, X. S. Zhao, C. Holm and M. Salanne, "Capacitance of Nanoporous Carbon-Based Supercapacitors Is a Trade-Off Between the Concentration and the Separability of the Ions", *Journal of Physical Chemistry Letters*, Vol. 7, No. 19, pp. 4015–4021, 2016.

54. Bates, J., F. Markoulidis, C. Lekakou and G. M. Laudone, "Design of Porous Carbons for Supercapacitor Applications for Different Organic Solvent-Electrolytes", *C*, Vol. 7, No. 1, p. 15, 2021.

55. Zhang, Y. and P. T. Cummings, "Effects of Solvent Concentration on the Performance of Ionic-Liquid/Carbon Supercapacitors", *ACS Applied Materials and Interfaces*, Vol. 11, pp. 42680–42689, 2019.

56. Uralcan, B., I. A. Aksay, P. G. Debenedetti and D. T. Limmer, "Concentra-

tion Fluctuations and Capacitive Response in Dense Ionic Solutions", *Journal of Physical Chemistry Letters*, Vol. 7, No. 13, pp. 2333–2338, 2016.

57. Uralcan, B. and I. B. Uralcan, "Origin of Enhanced Performance in Nanoporous Electrical Double Layer Capacitors: Insights on Micropore Structure and Electrolyte Composition From Molecular Simulations", *ACS Applied Materials and Interfaces*, Vol. 14, No. 14, pp. 16800–16808, 2022.

58. Jiang, D. E. and J. Wu, "Unusual Effects of Solvent Polarity on Capacitance for Organic Electrolytes in a Nanoporous Electrode", *Nanoscale*, Vol. 6, No. 10, pp. 5545–5550, 2014.

59. Decaux, C., C. Matei Ghimbeu, M. Dahbi, M. Anouti, D. Lemordant, F. Béguin, C. Vix-Guterl and E. Raymundo-Piñero, "Influence of Electrolyte Ion-Solvent Interactions on the Performances of Supercapacitors Porous Carbon Electrodes", *Journal of Power Sources*, Vol. 263, pp. 130–140, 2014.

60. Osti, N. C., K. L. Van Aken, M. W. Thompson, F. Tiet, D. E. Jiang, P. T. Cummings, Y. Gogotsi and E. Mamontov, "Solvent Polarity Governs Ion Interactions and Transport in a Solvated Room-Temperature Ionic Liquid", *Journal of Physical Chemistry Letters*, Vol. 8, No. 1, pp. 167–171, 2017.

61. Zhang, S., Z. Bo, H. Yang, J. Yang, L. Duan, J. Yan and K. Cen, "Insights Into the Effects of Solvent Properties in Graphene-Based Electric Double-Layer Capacitors With Organic Electrolytes", *Journal of Power Sources*, Vol. 334, pp. 162–169, 2016.

62. Lu, H., J. Zhou, Y. Cao, T. Shang, G. Ye, Q. H. Yang and X. Zhou, "Understanding the Effects of Electrode Meso-Macropore Structure and Solvent Polarity on Electric Double-Layer Capacitors Based on a Continuum Model", *Chinese Journal of Chemical Engineering*, Vol. 50, pp. 423–434, 2022.

63. Xu, C., J. Zhu, D. Li, X. Qian, G. Chen and H. Yang, "Unveiling the Effects of Solvent Polarity Within Graphene-Based Electric Double-Layer Capacitors", *Energies*, Vol. 15, No. 24, p. 9487, 2022.

64. Smith, A. M., A. A. Lee and S. Perkin, "The Electrostatic Screening Length in Concentrated Electrolytes Increases With Concentration", *Journal of Physical Chemistry Letters*, Vol. 7, No. 12, pp. 2157–2163, 2016.

65. Lee, A. A., C. S. Perez-Martinez, A. M. Smith and S. Perkin, "Scaling Analysis of the Screening Length in Concentrated Electrolytes", *Physical Review Letters*, Vol. 119, No. 2, p. 026002, 2017.

66. Coles, S. W., C. Park, R. Nikam, M. Kanduč, J. Dzubiella and B. Rotenberg, "Correlation Length in Concentrated Electrolytes: Insights From All-Atom Molecular Dynamics Simulations", *Journal of Physical Chemistry B*, Vol. 124, No. 9, pp. 1778–1786, 2020.

67. Fedorov, M. V. and A. A. Kornyshev, "Ionic Liquids at Electrified Interfaces", *Chemical Reviews*, Vol. 114, No. 5, pp. 2978–3036, 2014.

68. Merlet, C., B. Rotenberg, P. A. Madden, P.-L. Taberna, P. Simon, Y. Gogotsi and M. Salanne, "On the Molecular Origin of Supercapacitance in Nanoporous Carbon Electrodes", *Nature Materials*, Vol. 11, No. 4, pp. 306–310, 2012.

69. Feng, G., S. Li, V. Presser and P. T. Cummings, "Molecular Insights Into Carbon Supercapacitors Based on Room-Temperature Ionic Liquids", *The Journal of Physical Chemistry Letters*, Vol. 4, No. 19, pp. 3367–3376, 2013.

70. Vatamanu, J. and O. Borodin, "Ramifications of Water-in-Salt Interfacial Structure at Charged Electrodes for Electrolyte Electrochemical Stability", *The Journal of Physical Chemistry Letters*, Vol. 8, No. 18, pp. 4362–4367, 2017.

71. Vatamanu, J., O. Borodin, M. Olguin, G. Yushin and D. Bedrov, "Charge Storage

at the Nanoscale: Understanding the Trends From the Molecular Scale Perspective", *Journal of Materials Chemistry A*, Vol. 5, No. 40, pp. 21049–21076, 2017.

72. Largeot, C., C. Portet, J. Chmiola, P.-L. Taberna, Y. Gogotsi and P. Simon, "Relation Between the Ion Size and Pore Size for an Electric Double-Layer Capacitor", *Journal of the American Chemical Society*, Vol. 130, No. 9, pp. 2730–2731, 2008.

73. Shim, Y., Y. Jung and H. J. Kim, "Graphene-Based Supercapacitors: A Computer Simulation Study", *Journal of Physical Chemistry C*, Vol. 115, No. 47, pp. 23574–23583, 2011.

74. Li, D.-D., E.-C. Li, Y.-R. Yang, X.-D. Wang and G. Feng, "Structure and Capacitance of Electrical Double Layers in Tricationic Ionic Liquids With Organic Solvents", *The Journal of Physical Chemistry B*, Vol. 125, No. 46, pp. 12753–12762, 2021.

75. Limmer, D. T., "Interfacial Ordering and Accompanying Divergent Capacitance at Ionic Liquid-Metal Interfaces", *Physical Review Letters*, Vol. 115, No. 25, p. 256102, 2015.

76. Wang, Z., Y. Yang, D. L. Olmsted, M. Asta and B. B. Laird, "Evaluation of the Constant Potential Method in Simulating Electric Double-Layer Capacitors", *The Journal of Chemical Physics*, Vol. 141, No. 18, p. 184102, 2014.

77. Roy, D. and M. Maroncelli, "An Improved Four-Site Ionic Liquid Model", *The Journal of Physical Chemistry B*, Vol. 114, No. 39, pp. 12629–12631, 2010.

78. Duncan, M. F. E., P. A. Madden and I. R. McDonald, "A Computer Simulation Study of the Dielectric Properties of a Model of Methyl Cyanide", *Molecular Physics*, Vol. 51, No. 5, pp. 1141–1161, 1984.

79. Andersen, H. C., "RATTLE: A Velocity Version of the SHAKE Algorithm for Molecular Dynamics Calculations", *Journal of Computational Physics*, Vol. 52,

No. 1, pp. 24–34, 1983.

80. Thompson, A. P., H. M. Aktulga, R. Berger, D. S. Bolintineanu, W. M. Brown, P. S. Crozier, P. J. in 't Veld, A. Kohlmeyer, S. G. Moore, T. D. Nguyen, R. Shan, M. J. Stevens, J. Tranchida, C. Trott and S. J. Plimpton, "LAMMPS - A Flexible Simulation Tool for Particle-Based Materials Modeling at the Atomic, Meso, and Continuum Scales", *Computer Physics Communications*, Vol. 271, p. 108171, 2022.

81. Chmiola, J., C. Largeot, P.-L. Taberna, P. Simon and Y. Gogotsi, "Monolithic Carbide-Derived Carbon Films for Micro-Supercapacitors", *Science*, Vol. 328, No. 5977, pp. 480–483, 2010.

82. Li, F., A. Ahmad, L. Xie, G. Sun, Q. Kong, F. Su, Y. Ma, Y. Chao, X. Guo, X. Wei and C.-M. Chen, "Phosphorus-Modified Porous Carbon Aerogel Microspheres as High Volumetric Energy Density Electrode for Supercapacitor", *Electrochimica Acta*, Vol. 318, pp. 151–160, 2019.

83. Kurzweil, P., J. Schottenbauer and C. Schell, "Past, Present and Future of Electrochemical Capacitors: Pseudocapacitance, Aging Mechanisms and Service Life Estimation", *Journal of Energy Storage*, Vol. 35, p. 102311, 2021.

84. Bittner, A., M. Zhu, Y. Yang, H. Waibel, M. Konuma, U. Starke and C. Weber, "Aging of Electrochemical Double Layer Capacitors", *Journal of Power Sources*, Vol. 203, pp. 262–273, 2012.

85. Chiba, K., T. Ueda, Y. Yamaguchi, Y. Oki, F. Shimodate and K. Naoi, "Electrolyte Systems for High Withstand Voltage and Durability I. Linear Sulfones for Electric Double-Layer Capacitors", *Journal of The Electrochemical Society*, Vol. 158, No. 8, p. A872, 2011.

86. Sitlapersad, R. S., A. R. Thornton and W. K. den Otter, "A Simple Efficient Algo-

rithm for Molecular Simulations of Constant Potential Electrodes", *The Journal of Chemical Physics*, Vol. 160, No. 3, p. 034107, 2024.

87. Schütter, C., A. Bothe and A. Balducci, "Mixtures of Acetonitrile and Ethyl Isopropyl Sulfone as Electrolytes for Electrochemical Double Layer Capacitors", *Electrochimica Acta*, Vol. 331, p. 135421, 2020.

88. Zhang, K., C. Wei, M. Zheng, J. Huang and G. Zhou, "From Molecular Simulations to Experiments: The Recent Development of Room Temperature Ionic Liquid-Based Electrolytes in Electric Double-Layer Capacitors", *Molecules*, Vol. 29, No. 6, p. 1246, 2024.

89. Köps, L., F. Kreth, A. Bothe and A. Balducci, "High Voltage Electrochemical Capacitors Operating at Elevated Temperature Based on 1,1-Dimethylpyrrolidinium Tetrafluoroborate", *Energy Storage Materials*, Vol. 44, pp. 66–72, 2022.

90. Iro, Z. S., C. Subramani and S. S. Dash, "A Brief Review on Electrode Materials for Supercapacitor", *International Journal of Electrochemical Science*, Vol. 11, No. 12, pp. 10628–10643, 2016.

91. Li, X., H. Song, Y. Zhang, H. Wang, K. Du, H. Li, Y. Yuan and J. Huang, "Enhanced Electrochemical Capacitance of Graphene Nanosheets Coating With Polyaniline for Supercapacitors", *International Journal of Electrochemical Science*, Vol. 7, No. 6, pp. 5163–5171, 2012.

92. Lach, J., K. Wróbel, J. Wróbel, P. Podsadni and A. Czerwiński, "Applications of Carbon in Lead-Acid Batteries: A Review", *Journal of Solid State Electrochemistry*, Vol. 23, No. 8, p. 693–705, 2019.

93. Roy, D., N. Patel, S. Conte and M. Maroncelli, "Dynamics in an Idealized Ionic Liquid Model", *The Journal of Physical Chemistry B*, Vol. 114, No. 25, pp. 8410–8424, 2010.

94. Cole, M. W. and J. R. Klein, "The Interaction Between Noble Gases and the Basal Plane Surface of Graphite", *Surface Science*, Vol. 124, No. 2, pp. 547–554, 1983.

95. Pal, B., S. Yang, S. Ramesh, V. Thangadurai and R. Jose, "Electrolyte Selection for Supercapacitive Devices: A Critical Review", *Nanoscale Advances*, Vol. 1, No. 10, pp. 3807–3835, 2019.

96. Yu, L. and G. Z. Chen, "Ionic liquid-based electrolytes for supercapacitor and supercapattery", , 2019.

97. Kaya, D., D. Koroglu, E. Aydın and B. Uralcan, "Optimization of Capacitance in Supercapacitors by Constructing an Experimentally Validated Hybrid Artificial Neural Networks-Genetic Algorithm Framework", *Journal of Power Sources*, Vol. 568, p. 232987, 2023.

98. Noh, C. and Y. Jung, "Understanding the Charging Dynamics of an Ionic Liquid Electric Double Layer Capacitor: Via Molecular Dynamics Simulations", *Physical Chemistry Chemical Physics*, Vol. 21, No. 13, pp. 6790–6800, 2019.

99. Bi, S., H. Banda, M. Chen, L. Niu, M. Chen, T. Wu, J. Wang, R. Wang, J. Feng, T. Chen, M. Dincă, A. A. Kornyshev and G. Feng, "Molecular Understanding of Charge Storage and Charging Dynamics in Supercapacitors With MOF Electrodes and Ionic Liquid Electrolytes", *Nature Materials*, Vol. 19, No. 5, pp. 552–558, 2020.

100. McDaniel, J. G. and C. Y. Son, "Ion Correlation and Collective Dynamics in BMIM/BF4-Based Organic Electrolytes: From Dilute Solutions to the Ionic Liquid Limit", *The Journal of Physical Chemistry B*, Vol. 122, No. 28, pp. 7154–7169, 2018.

101. Vasilyev, O., A. Kornyshev and S. Kondrat, "Connections Matter: On the Impor-

tance of Pore Percolation for Nanoporous Supercapacitors", *ACS Applied Energy Materials*, Vol. 2, No. 8, pp. 5386–5390, 2019.

102. Joshi, S. Y. and S. A. Deshmukh, "A Review of Advancements in Coarse-Grained Molecular Dynamics Simulations", *Molecular Simulation*, Vol. 47, No. 10-11, pp. 786–803, 2021.

103. Martini, A., S. J. Eder and N. Dörr, "Tribochemistry: A Review of Reactive Molecular Dynamics Simulations", *Lubricants*, Vol. 8, No. 4, p. 44, 2020.

104. Largeot, C., C. Portet, J. Chmiola, P.-L. Taberna, Y. Gogotsi and P. Simon, "Relation Between the Ion Size and Pore Size for an Electric Double-Layer Capacitor", *Journal of the American Chemical Society*, Vol. 130, No. 9, pp. 2730–2731, 2008.

105. Kondrat, S., P. Wu, R. Qiao and A. A. Kornyshev, "Accelerating Charging Dynamics in Subnanometer Pores", *Nature Materials*, Vol. 13, No. 4, pp. 387–393, 2014.

APPENDIX A: ANALYSIS RESULTS

All Python codes and data that are used in this study can be found in the following link: `https://drive.google.com/drive/folders/1l4qCPUmPdHkbKeSRo2fBsu_RHyI96b74?usp=sharing`

A.1. Charging Profiles

In Figure A.1, time evolutions of the total positive electrode charge are given.

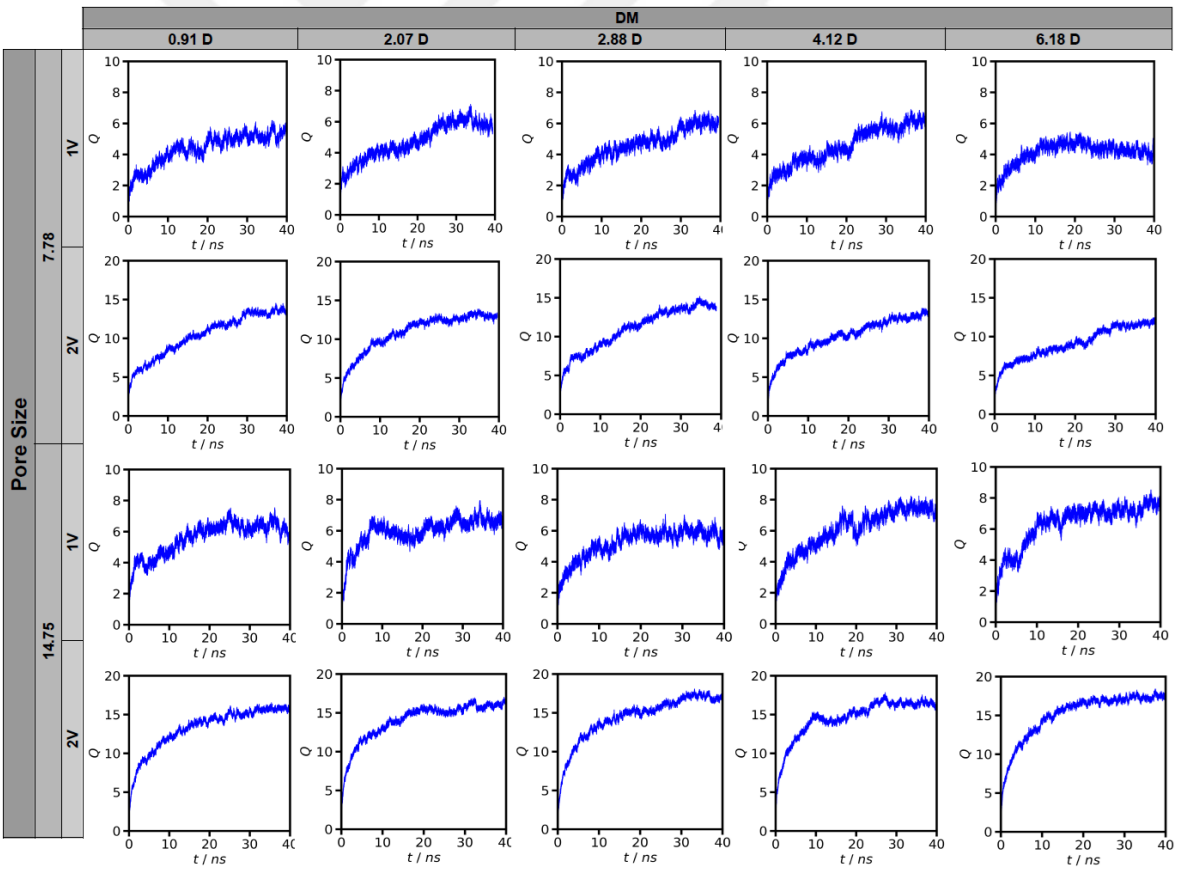

Figure A.1. Time evolution of total charge of the positive electrodes for all systems.

A.2. Ion Polarization

In Figure A.2, time evolutions of the ion polarization of positively charged electrode are given.

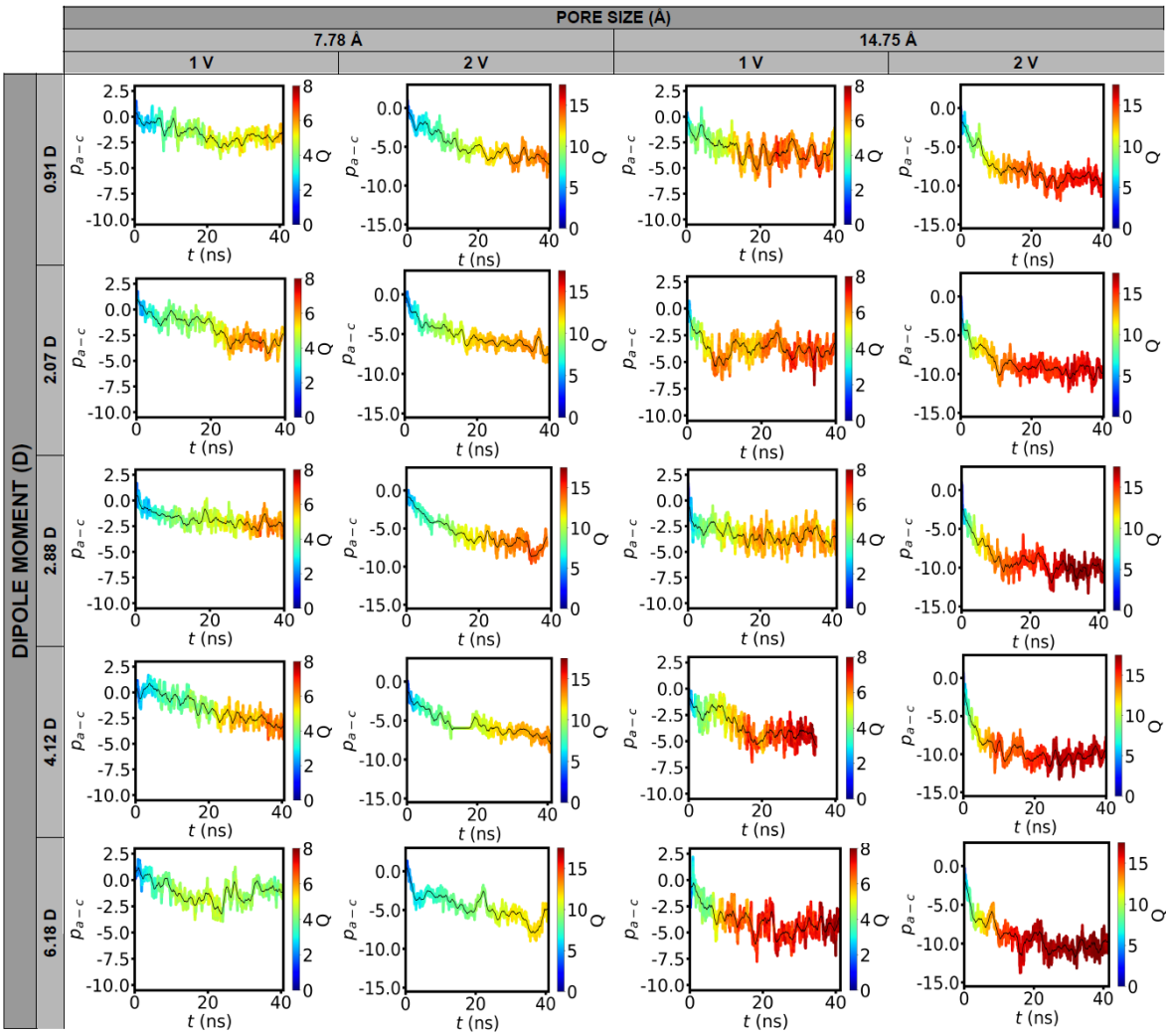

Figure A.2. Time evolution of ion polarization and total positive electrode charge for all systems.

A.3. Number Density Profiles

In Figure A.3 and Figure A.4, number density profiles of EDLC systems are given.

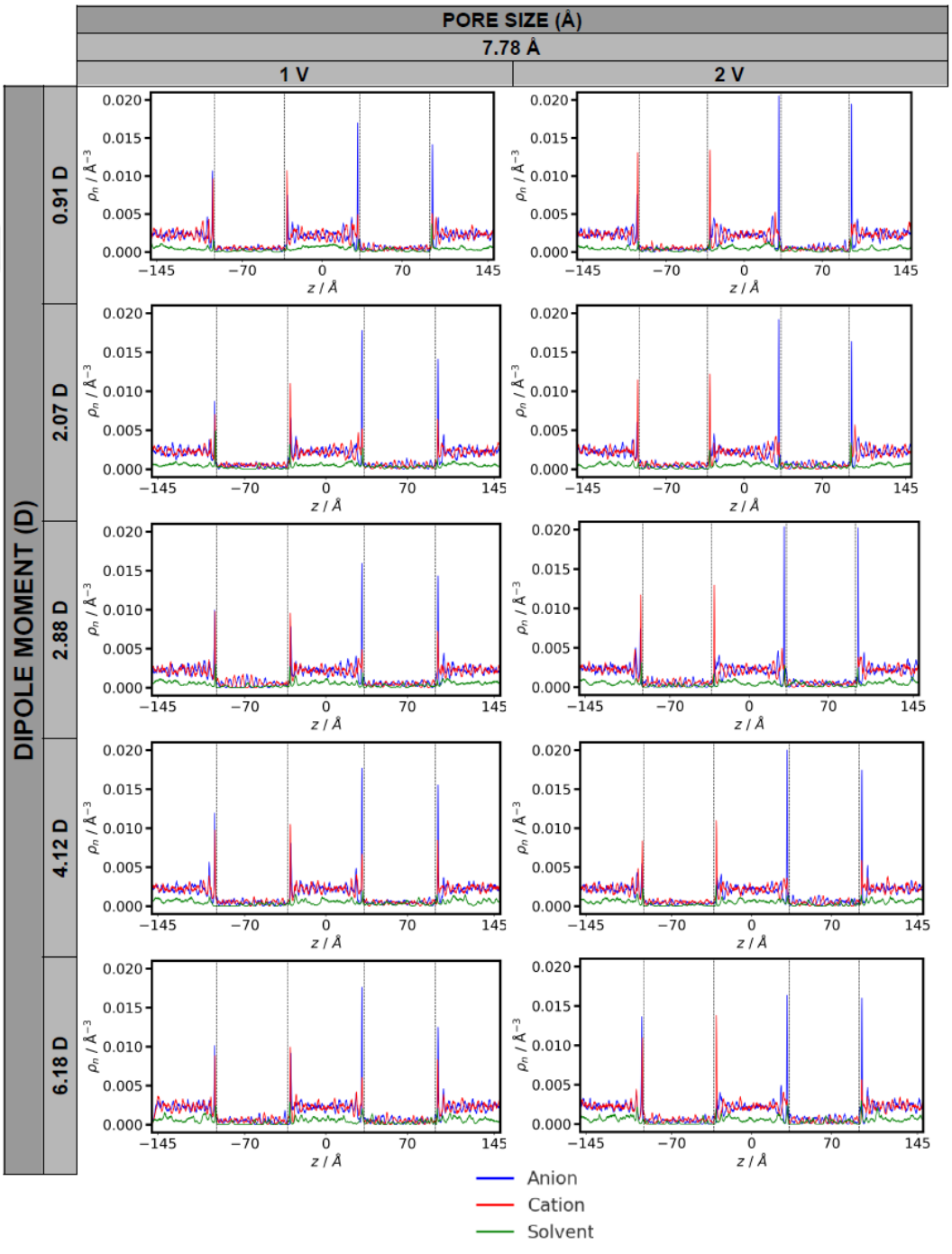

Figure A.3. Number density profiles along $\hat{z}$, for systems with a 7.78 Å pore.

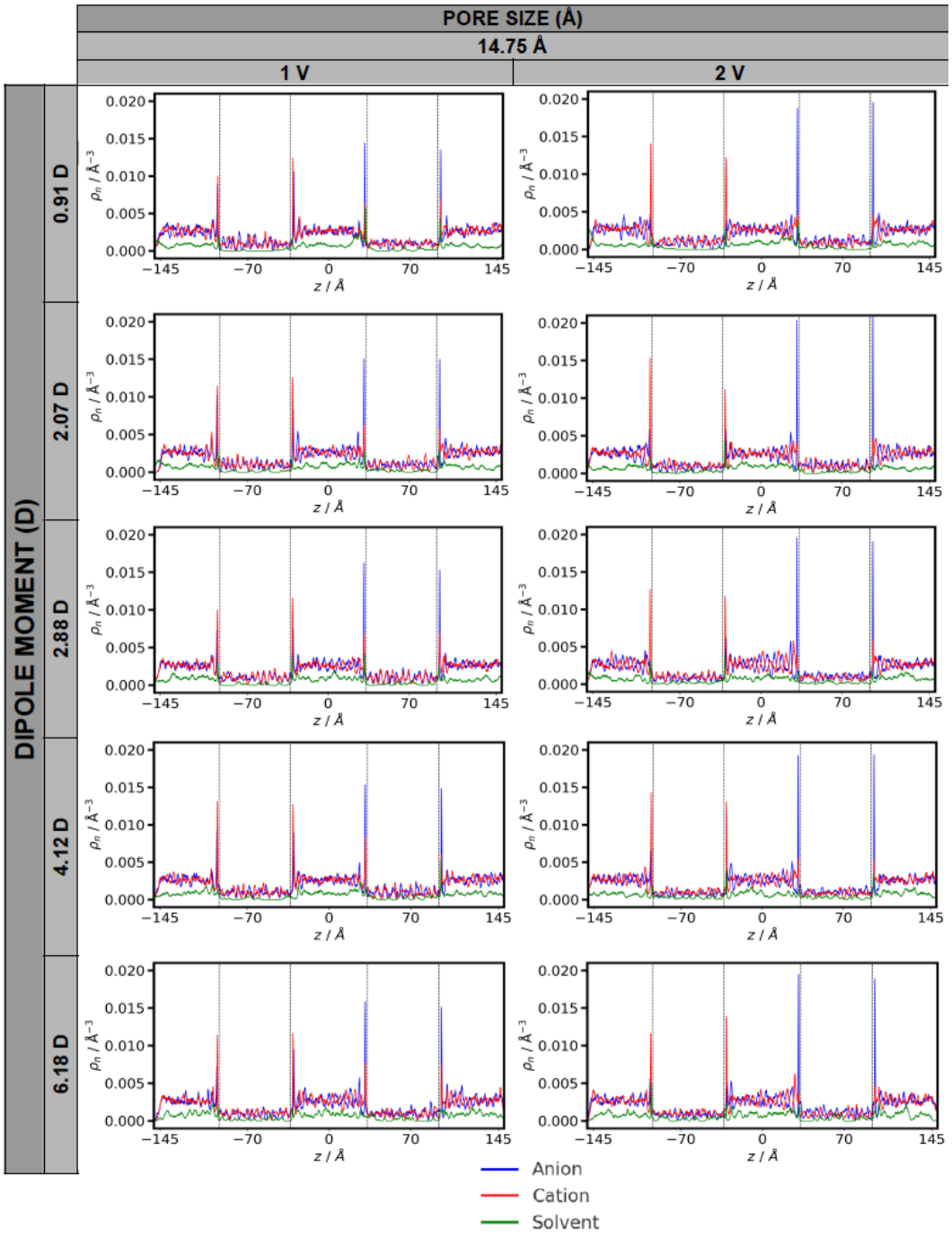

Figure A.4. Number density profiles along $\hat{z}$, for systems with a 14.75 Å pore.

A.4. Charge Density Profiles

In Figure A.5 and Figure A.6, charge density profiles of EDLC systems are given.

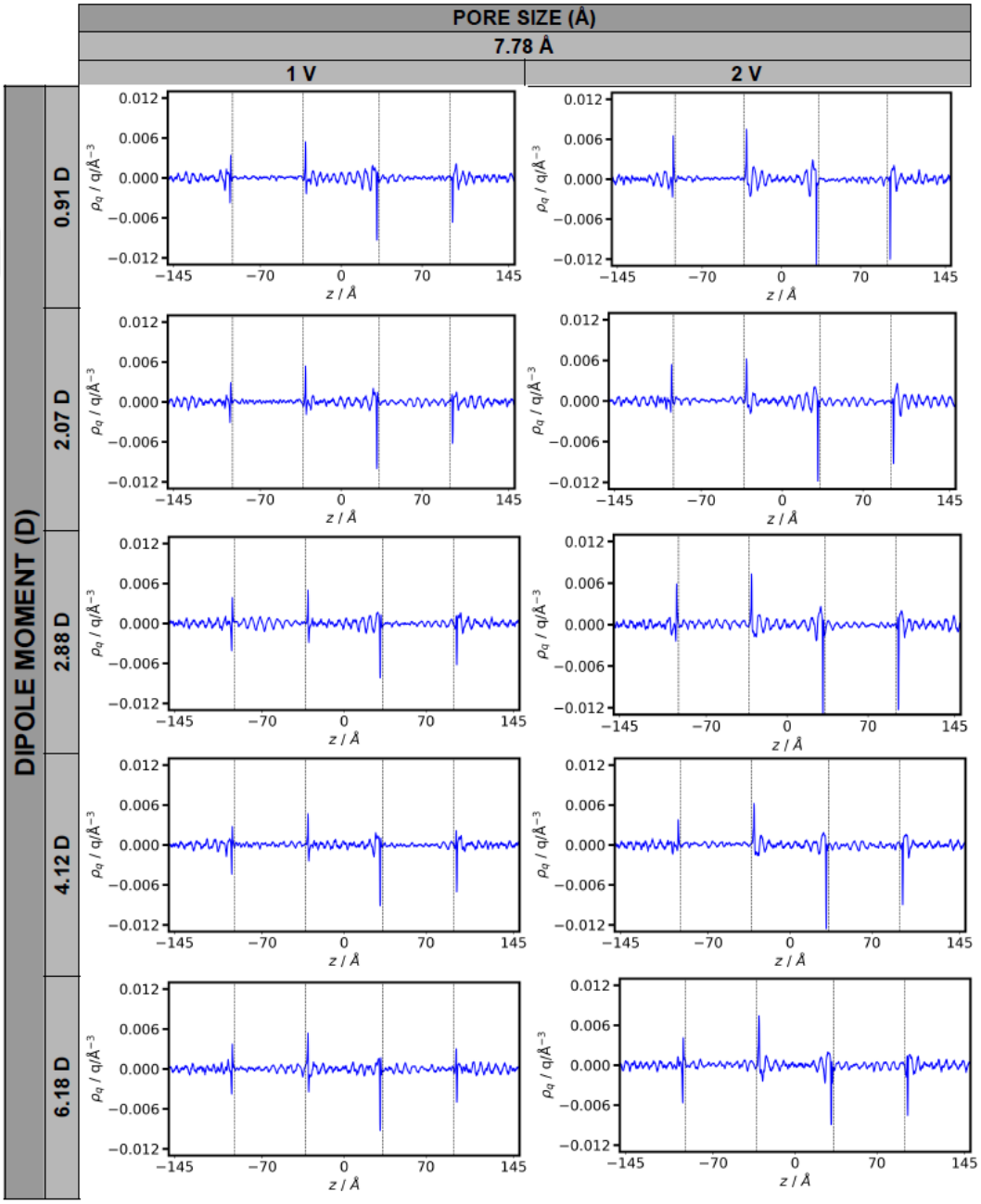

Figure A.5. Charge density profiles along $\hat{z}$, for systems with a 7.78 Å pore.

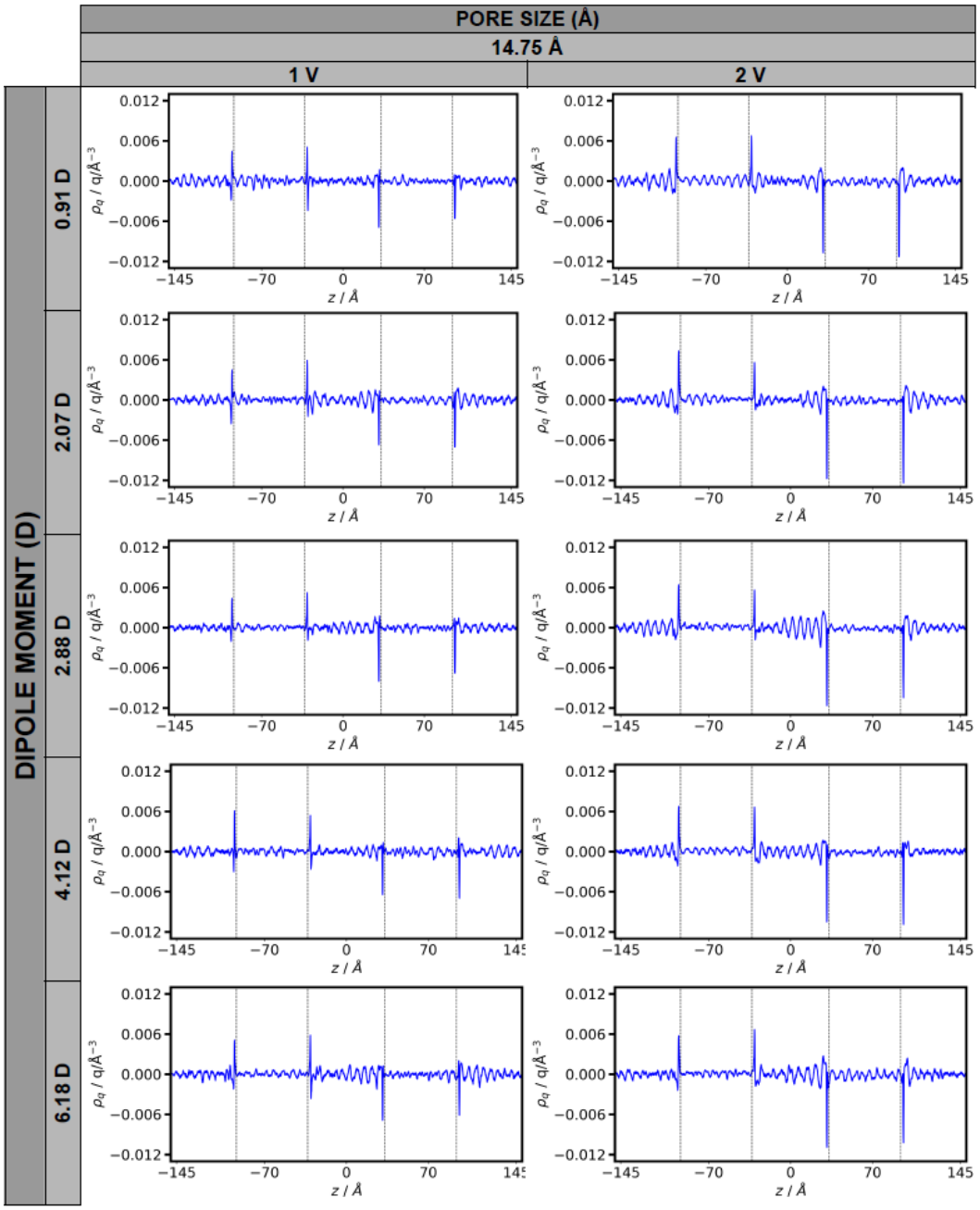

Figure A.6. Charge density profiles along $\hat{z}$, for systems with a 14.75 Å pore.

A.5. Free Energy Profiles

In Figure A.7 and Figure A.8, free energy profiles of EDLC systems are given.

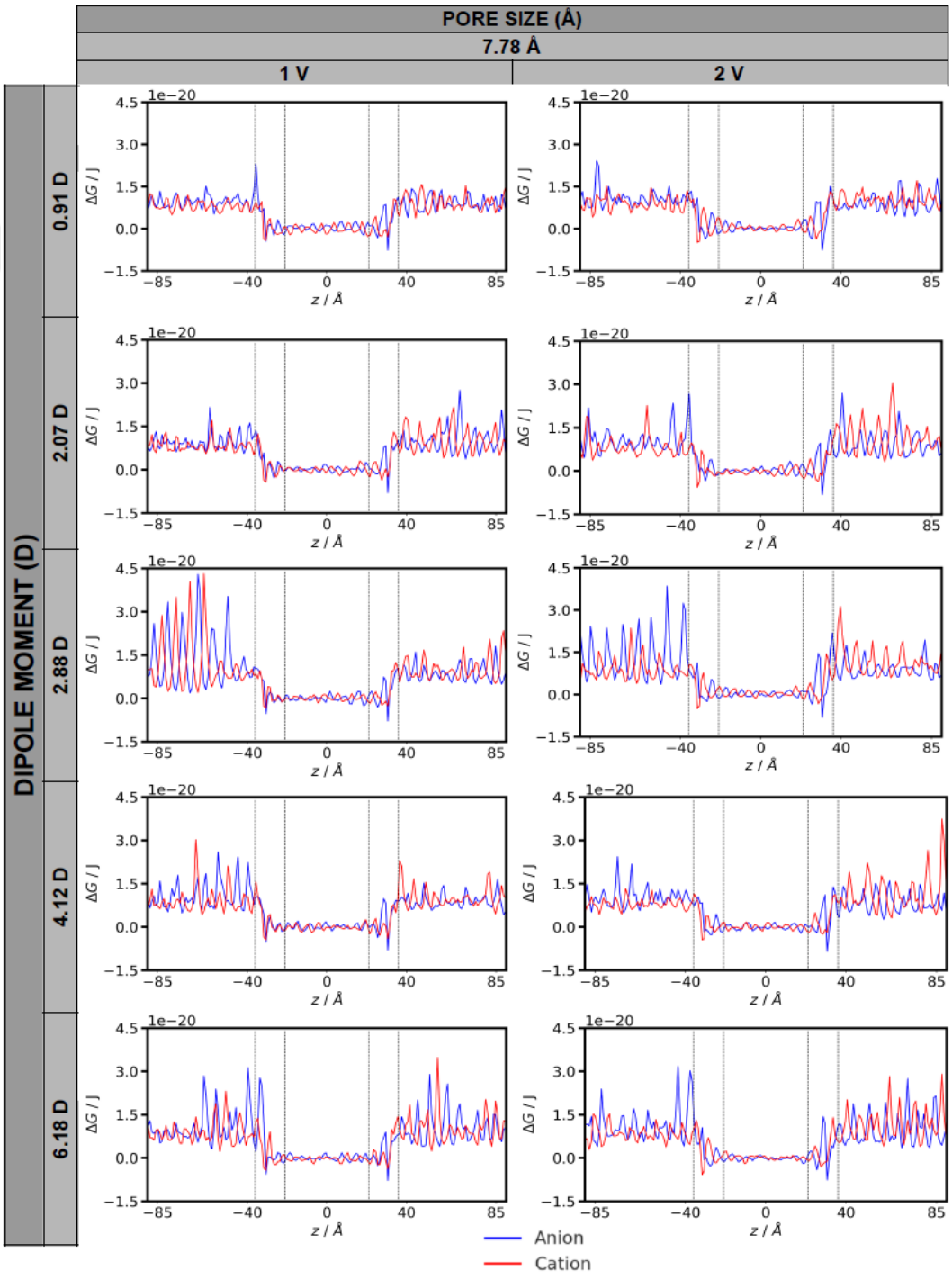

Figure A.7. Free energy profiles along $\hat{z}$, for systems with a 7.78 Å pore.

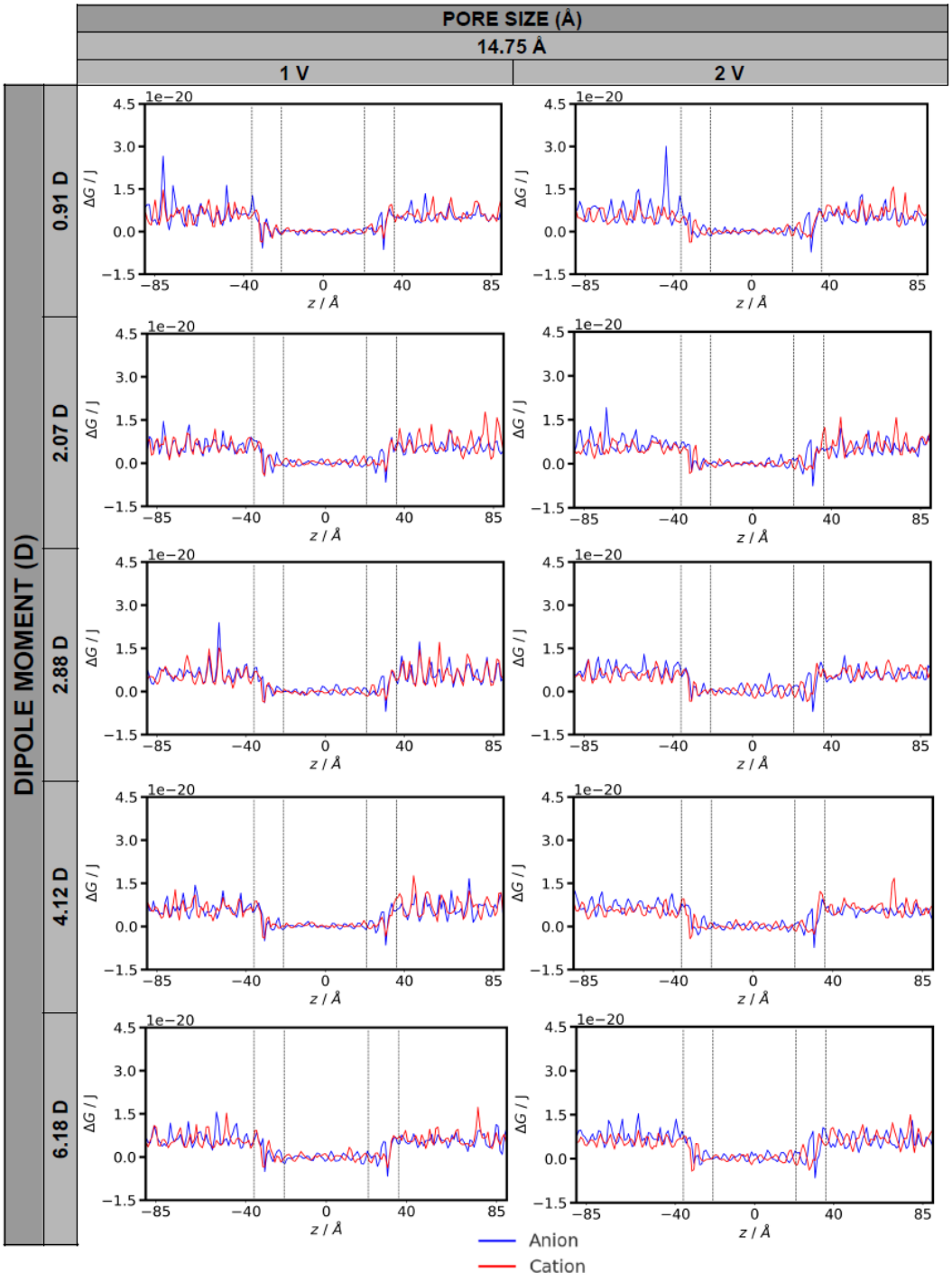

Figure A.8. Free energy profiles along $\hat{z}$, for systems with a 14.75 Å pore.